

Supporting Information for:

The Role of the Droplet Interface in Controlling the Multiphase Oxidation of Thiosulfate by Ozone

Alexandra M. Deal¹, Franky Bernal^{1,2}, Andreas Siebert^{1,3}, Alexander M. Prophet^{1,2},
Mauricio Lopez Luna¹, Monika Blum^{1,3}, Richard J. Saykally^{1,2}, and Kevin R. Wilson^{1,*}

¹*Chemical Sciences Division, Lawrence Berkeley National Laboratory, Berkeley, CA 94720, United States*

²*Department of Chemistry, University of California, Berkeley, Berkeley, CA 94720, United States*

³*Advanced Light Source, Lawrence Berkeley National Laboratory, Berkeley, CA 94720, United States*

**Corresponding Author; krwilson@lbl.gov*

Table of Contents

S1. Kinetic Modeling Information.....	2
S1.1. SO ₂ Equilibria and Evaporation.....	4
S1.2. 2-Compartment and 3-Compartment Models.....	6
S1.3. Comparison Between Two-Compartment and Three-Compartment Models.....	8
S2. Liquid Flat Jet APXPS Measurements.....	9
S2.1. Experimental Methods.....	9
S2.2. O 1s Core Level Fits.....	10
S2.3. Thiosulfate (S ₂ O ₃ ²⁻) surface concentration.....	13
S3. Constraining [S ₂ O ₃ ^{2-(ads)}] _{max} Using DUV-SHG and APXPS Experiments.....	15
S4. DUV-SHG of Thiosulfate at pH 13.....	20
S5. Agreement Between Experimental Data and Kinetic Model Predictions.....	22
S6. Comparison Between Modeled Kinetics and All Data Reported by Hsu, <i>et al.</i> ³⁷	24
S7. Levitated Droplets Experimental Schematic.....	28
S8. Calculated Ozone Concentration Near the Interface.....	29
S9. 3-Compartment Model Comparisons for Figure 8.....	30
S10. Average Sulfur Oxidation States for a Range of Droplet Sizes and Concentrations.....	32
References.....	33

S1. Kinetic Modeling Information

Table S1. Elementary Reaction Steps, Reaction Rate Constants, and Diffusion Coefficients used in Kinetiscope© Simulations. Recreated from Ref ¹

#	Step	Rate Constant or Diffusion Coefficient ^o	Reference(s)
S1	$O_{3(diff)} + site_{O_3} \xrightleftharpoons[k_{des}]{k_{ads}} O_{3(ads)}$	$k_{ads} = 1.77 \times 10^{-11} \cdot [O_{3(g)}] s^{-1}$ $k_{des} = 1.93 \times 10^{10} s^{-1}$	² See section 2.1.1.
S2	$O_{3(ads)} \xrightleftharpoons[k_{desolv}]{k_{solv}} O_{3(b)} + site_{O_3}$	$k_{solv} = 1.90 \times 10^8 \cdot s^{-1}$ $k_{desolv} = 1.20 \times 10^{-12} cm^3 \cdot molec^{-1} \cdot s^{-1}$	² See section 2.1.1.
S3	$S_2O_{3(ads)}^{2-} + O_{3(ads)} \xrightarrow{k_{STS}} [S_2O_3OOO]_{(ads)}^{2-} + site_{O_3}$	$k_{STS} = 1.20 \times 10^{-13} cm^3 \cdot molec^{-1} \cdot s^{-1}$	³
S4	$[S_2O_3OOO]_{(ads)}^{2-} + H^+ + site_{SO_2} \xrightarrow{k_{1a}} SO_{4(ads)}^{2-}$	$k_{1a} = k_{Hdiff} \cdot [H^+] s^{-1}$	See note *
S5	$[S_2O_3OOO]_{(ads)}^{2-} \xrightarrow{k_{1b}} S_2O_{4(ads)}^{2-} + O_2$	$k_{1b} = 1 \times 10^5 s^{-1}$	¹
S6	$[S_2O_3OOO]_{(ads)}^{2-} + H^+ \xrightarrow{k_{1c}} HS_2O_{4(ads)}^{2-} + O_2$	$k_{1c} = k_{Hdiff} \cdot [H^+] s^{-1}$	See note *
S7	$S_2O_{4(ads)}^{2-} + H^+ \xrightleftharpoons[k_b]{k_f} HS_2O_{4(ads)}^{2-}$	$k_f = k_{Hdiff} \cdot [H^+] s^{-1}$ $k_b = 3.6 \times 10^8 s^{-1}$	⁴ See note *, †
S8	$S_2O_{4(ads)}^{2-} + O_{2(surf)} + site_{SO_2} \xrightarrow{k_{3a}} SO_{4(ads)}^{2-} + site_{SO_2}$	$k_{2a} = k_e^0 \cdot [O_{2(surf)}]$ $k_e^0 = 8 \times 10^{-11} (cm^3)^{0.5} \cdot molec^{-1/2} \cdot s^{-1}$	^{1, 5}
S9	$S_2O_{4(ads)}^{2-} + SO_{2(ads)} \xrightarrow{k_{3b}} S_3O_{6(ads)}^{2-} + site_{SO_2}$	$k_{2b} = 1 \times 10^{-12} cm^3 \cdot molec^{-1} \cdot s^{-1}$	¹
S10	$HS_2O_{4(ads)}^{2-} + S_2O_{3(ads)} \xrightarrow{k_{3c}} S_3O_{6(ads)}^{2-} + OH^-$	$k_{2c} = 1 \times 10^{-19} cm^3 \cdot molec^{-1} \cdot s^{-1}$	¹
S11	$SO_{2(ads)} \xrightarrow{k_{des}} SO_{2(gas)} + site_{SO_2}$	$k_{des} = 3.70 \times 10^7 s^{-1}$	See Section S1.1.
S12	$SO_{2(ads)} + H_2O + site_{SO_3} \xrightleftharpoons[k_{bT}]{k_{fT}} SO_{3(ads)}^{2-} + 2H^+$	$k_{fT} = \frac{K_{a1}K_{a2}k_{b2}}{[H^+]} s^{-1}$ $k_{bT} = \frac{k_{b1}[H^+]^2}{K_{a2}} s^{-1}$ $pK_{a1} = 1.9; pK_{a2} = 7.2$ $k_{b1} = k_{b2} = k_{Hdiff}$	⁶⁻⁹ See Section S1.1.
S13	$SO_{3(ads)}^{2-} + O_{3(ads)} \xrightarrow{k_{SO_3,eff}} SO_{4(ads)}^{2-} + site_{O_3}$	$pH 5: k_{SO_3,eff} = 1.1 \times 10^{-14} cm^3 \cdot molec^{-1} \cdot s^{-1}$ $pH 9: k_{SO_3,eff} = 1.6 \times 10^{-12} cm^3 \cdot molec^{-1} \cdot s^{-1}$ $pH 13: k_{SO_3,eff} = 1.7 \times 10^{-12} cm^3 \cdot molec^{-1} \cdot s^{-1}$	⁸
S14	$S_2O_{3(ads)}^{2-} \xrightleftharpoons[k_{desolv}]{k_{solv}} S_2O_{3(b)}^{2-} + site_{O_3}$	$k_{solv} = 1.0 \times 10^3 \cdot s^{-1}$ $k_{desolv} = 5.9 \times 10^{-19} cm^3 \cdot molec^{-1} \cdot s^{-1}$	¹
S15	$[S_2O_3OOO]_{(bulk)}^{2-} + site_{O_3} \xrightarrow{k_{desolv}} [S_2O_3OOO]_{(ads)}^{2-}$	$k_{desolv} = 1.0 \times 10^{-15} cm^3 \cdot molec^{-1} \cdot s^{-1}$	See note ^l

S16	$S_2O_{4(ads)}^{2-} \xrightleftharpoons[k_{desolv}]{k_{solv}} S_2O_{4(b)}^{2-} + site$	$k_{solv} = 1.0 \times 10^3 \cdot s^{-1}$ $k_{desolv} = 5.9 \times 10^{-18} \text{ cm}^3 \cdot \text{molec}^{-1}$	See section 2.1.2.
S17	$HS_2O_{4(ads)}^- \xrightleftharpoons[k_{desolv}]{k_{solv}} HS_2O_{4(b)}^- + site$	$k_{solv} = 1.0 \times 10^3 \cdot s^{-1}$ $k_{desolv} = 5.9 \times 10^{-19} \text{ cm}^3 \cdot \text{molec}^{-1}$	See section 2.1.2.
S18	$SO_{2(ads)} \xrightleftharpoons[k_{desolv}]{k_{solv}} SO_{2(b)} + site$	$k_{solv} = 4.6 \times 10^6 \cdot s^{-1}$ $k_{desolv} = 3.3 \times 10^{-14} \text{ cm}^3 \cdot \text{molec}^{-1}$	See section 2.1.1.
S19	$SO_{3(ads)}^{2-} \xrightleftharpoons[k_{desolv}]{k_{solv}} SO_{3(b)}^{2-} + site$	$k_{solv} = 1.0 \times 10^3 \cdot s^{-1}$ $k_{desolv} = 5.9 \times 10^{-20} \text{ cm}^3 \cdot \text{molec}^{-1}$	¹⁰ , See section 2.1.2.
S20	$SO_{4(ads)}^{2-} \xrightleftharpoons[k_{desolv}]{k_{solv}} SO_{4(b)}^{2-} + site$	$k_{solv} = 1.0 \times 10^3 \cdot s^{-1}$ $k_{desolv} = 5.9 \times 10^{-20} \text{ cm}^3 \cdot \text{molec}^{-1}$	¹¹ , See section 2.1.2.
S21	$S_3O_{6(ads)}^{2-} \xrightleftharpoons[k_{desolv}]{k_{solv}} S_3O_{6(b)}^{2-} + site$	$k_{solv} = 1.0 \times 10^3 \cdot s^{-1}$ $k_{desolv} = 5.9 \times 10^{-19} \text{ cm}^3 \cdot \text{molec}^{-1}$	See section 2.1.2.
S22	$S_4O_{6(ads)}^{2-} \xrightleftharpoons[k_{desolv}]{k_{solv}} S_4O_{6(b)}^{2-} + site$	$k_{solv} = 1.0 \times 10^3 \cdot s^{-1}$ $k_{desolv} = 5.9 \times 10^{-19} \text{ cm}^3 \cdot \text{molec}^{-1}$	See section 2.1.2.
D1	$O_{3(b)}$	$D = 1.76 \times 10^{-5} \text{ cm}^2 \cdot \text{s}^{-1}$	¹²
D2	$S_2O_{3(b)}^{2-}$	$D = 8 \times 10^{-6} \text{ cm}^2 \cdot \text{s}^{-1}$	See note [§]
D3	$[S_2O_3OOO]_{(bulk)}^{2-}$	$D = 8 \times 10^{-6} \text{ cm}^2 \cdot \text{s}^{-1}$	See note [§]
D4	$S_2O_{4(ads)}^{2-}$	$D = 8 \times 10^{-6} \text{ cm}^2 \cdot \text{s}^{-1}$	See note [§]
D5	$HS_2O_{4(ads)}^-$	$D = 8 \times 10^{-6} \text{ cm}^2 \cdot \text{s}^{-1}$	See note [§]
D6	$SO_{2(b)}$	$D = 1.83 \times 10^{-5} \text{ cm}^2 \cdot \text{s}^{-1}$	¹³
D7	$SO_{3(b)}^{2-}$	$D = 9.59 \times 10^{-6} \text{ cm}^2 \cdot \text{s}^{-1}$	¹³
D8	$SO_{4(b)}^{2-}$	$D = 8.33 \times 10^{-6} \text{ cm}^2 \cdot \text{s}^{-1}$	¹⁴
D10	$S_3O_{6(b)}^{2-}$	$D = 8 \times 10^{-6} \text{ cm}^2 \cdot \text{s}^{-1}$	See note [§]
D11	$S_4O_{6(b)}^{2-}$	$D = 8 \times 10^{-6} \text{ cm}^2 \cdot \text{s}^{-1}$	See note [§]
B1	$S_2O_{3(b)}^{2-} + O_{3(b)} \xrightarrow{k_{STS}} [S_2O_3OOO]_{(b)}^{2-}$	$k_{STS} = 1.20 \times 10^{-13} \text{ cm}^3 \cdot \text{molec}^{-1} \cdot \text{s}^{-1}$	³
B2	$[S_2O_3OOO]_{(b)}^{2-} + H^+ \xrightarrow{k_{1a}} SO_{4(b)}^{2-} + SO_{2(b)} + H$	$k_{1a} = k_{Hdiff} \cdot [H^+] \text{ s}^{-1}$	See note *
B3	$[S_2O_3OOO]_{(b)}^{2-} \xrightarrow{k_{1b}} S_2O_{4(b)}^{2-} + O_2$	$k_{1b} = 1 \times 10^5 \text{ s}^{-1}$	¹
B4	$[S_2O_3OOO]_{(b)}^{2-} + H^+ \xrightarrow{k_{1c}} HS_2O_{4(b)}^{2-} + O_2$	$k_{1c} = k_{Hdiff} \cdot [H^+] \text{ s}^{-1}$	See note *
B5	$S_2O_{4(b)}^{2-} + H^+ \xrightleftharpoons[k_b]{k_f} HS_2O_{4(b)}^{2-}$	$k_f = k_{Hdiff} \cdot [H^+] \text{ s}^{-1}$ $k_b = 3.6 \times 10^8 \text{ s}^{-1}$	⁴ See note *, [‡]
B6	$S_2O_{4(b)}^{2-} + O_{2(b)} \xrightarrow{k_{3a}} SO_{4(b)}^{2-} + SO_2$	$k_{2a} = k_e^0 \cdot [O_{2(b)}]$ $k_e^0 = 8.0 \times 10^{-11} (\text{cm}^3)^{1/2} \cdot \text{molec}^{-1}$	^{1, 5}
B7	$S_2O_{4(b)}^{2-} + SO_{2(b)} \xrightarrow{k_{3b}} S_3O_{6(b)}^{2-}$	$k_{2b} = 1 \times 10^{-12} \text{ cm}^3 \cdot \text{molec}^{-1} \cdot \text{s}^{-1}$	¹
B8	$HS_2O_{4(b)}^- + S_2O_{3(b)} \xrightarrow{k_{3c}} S_3O_{6(b)}^{2-} + OH^-$	$k_{2c} = 1 \times 10^{-19} \text{ cm}^3 \cdot \text{molec}^{-1} \cdot \text{s}^{-1}$	¹
B9	$SO_{2(b)} + H_2O \xrightleftharpoons[k_b]{k_f} SO_{3(b)}^{2-} + 2H^+$	$k_{fT} = \frac{K_{a1} K_{a2} k_{b2}}{[H^+]} \text{ s}^{-1}$	⁶⁻⁹ See Section S1.1

		$k_{bT} = \frac{k_{b1}[H^+]^2}{K_{a2}} s^{-1}$ $pK_{a1} = 1.9; pK_{a2} = 7.2$ $k_{b1} = k_{b2} = k_{Hdiff}$	
B10	$SO_{3(b)}^{2-} + O_{3(b)} \xrightarrow{k_{SO_3, eff}} SO_{4(b)}^{2-}$	$pH\ 5: k_{SO_3, eff} = 1.1 \times 10^{-14} cm^3 \cdot m^{-3} \cdot s^{-1}$ ⁸ $pH\ 9: k_{SO_3, eff} = 1.6 \times 10^{-12} cm^3 \cdot m^{-3} \cdot s^{-1}$ $pH\ 13: k_{SO_3, eff} = 1.7 \times 10^{-12} cm^3 \cdot m^{-3} \cdot s^{-1}$	

*[H⁺] is not explicitly defined in simulations. Instead, a pseudo-first order rate constant is used, assuming a constant [H⁺] calculated from the measured pH and assuming the upper limit for the rate constant of proton recombination, $k_{Hdiff} = 1.66 \times 10^{-11} cm^3 \cdot molec^{-1} \cdot s^{-1}$, measured previously.^{6,7}

†Acid equilibria are modeled using the pseudo-first order and diffusion limited assumptions shown in Note * for the forward rate. The literature value for the acid dissociation constant is used to calculate the backwards rate $k_b = K_a \cdot k_{Hdiff}$.

§To our knowledge, diffusivities of [S₂O₃OOO]²⁻, S₂O₄²⁻, HS₂O₄⁻, S₂O₃²⁻, S₃O₆²⁻, and S₄O₆²⁻ have not been measured, but we estimate that diffusivities for these species would be like those of SO₂, SO₃²⁻, and SO₄²⁻, and simulations are insensitive to the exact values used.

¶The thiosulfate-ozone complex is considered most stable at the interface, so no solvation step is included. Desolvation (step S16) is included so that the small amounts of the complex formed in the bulk will adsorb to the interface prior to reaction.

°Concentrations of sites are not included in the rate equations for reactions S1-S15, but these reactions cannot occur if there are no available sites of the type indicated.

S1.1. SO₂ Equilibria and Evaporation

Simulation results showed that the overall kinetics are sensitive to both the partitioning and equilibria of sulfur dioxide (SO₂). Once formed, SO₂ can adsorb to/desorb from the interface, evaporate from the interface into the gas-phase, or hydrolyze, forming an equilibrium with HSO₃⁻ and SO₃²⁻. Although the kinetics of SO₂ hydrolysis and its equilibrium with bisulfite/sulfite are well known, the gas-interface-bulk partitioning of SO₂ is harder to constrain.

Here, we model SO₂ as ozone is modeled, using a Langmuir framework for adsorption to the interface and the Henry's law components, H_{cc}^{gs} and H_{cc}^{sb} , for partitioning between the three regimes. To do this, we use literature values for the mass accommodation coefficient, α , surface excess, $\Gamma_{SO_2}^{\infty}$, gas-to-bulk Henry's law coefficient, H_{cc}^{gb} , and the Gibbs free energy for gas-to-interface adsorption, ΔG_{gs} . We test two mass accommodation coefficients: 0.110 as calculated by Worsnop, *et al.*¹⁵ and 0.175 as calculated by Boniface, *et al.*¹⁶ Sander⁷ provides multiple values

for H_{cc}^{gb} , ranging from 27 to 71, with most studies centering around values between 27 and 37. While many studies agree that SO_2 has a strong surface affinity,^{10, 16-19} determining the free energy for adsorption and the surface excess can be challenging due to the equilibrium between SO_2 , HSO_3^- , and SO_3^{2-} . Experimental and computational values for the gas to interface solvation free energy, ΔG_{gs} , range from -2.7 kcal/mol to -5.3 kcal/mol^{17, 18, 20, 21} and values for the surface excess, $\Gamma_{SO_2}^\infty$, range from 4.0×10^{14} molec·cm⁻² to 4.3×10^{15} molec·cm⁻².^{21, 22}

As summarized in Table S2, we can create an envelope for SO_2 partitioning by using this literature data to calculate minimum and maximum values for k_{des} , k_{solv} , and k_{desolv} . Following the framework used for ozone in this work and in previous work:^{2, 23}

$$k_{des} = \frac{k_{ads} \cdot \Gamma_{SO_2}^\infty}{H_{cc}^{gs} \cdot \delta}, \quad (1)$$

where $k_{ads} = \frac{1}{4} A \bar{c} \sigma$ ($cm^3 \cdot molec^{-1} \cdot s^{-1}$), $H_{cc}^{gs} = \exp\left(\frac{-\Delta G_{gs}}{RT}\right)$, δ is the thickness of the interface (1

nm), A is the area of the interface (1 nm x 1 nm), \bar{c} is the mean free speed of the SO_2 molecule in the gas-phase, and σ is the sticking coefficient (assumed to be 1 for simplicity). Given that we have a range of values for surface excess and adsorption free energy, we calculate a minimum

value of $k_{des}^{min} = 9.3 \times 10^6 s^{-1}$ using $\Gamma_{SO_2}^\infty = 4.0 \times 10^{14} molec \cdot cm^{-2}$ and $\Delta G_{gs} = -5.3 kcal/mol$ ($H_{cc}^{gs} = 8,400$)

and a maximum value of $k_{des}^{max} = 3.4 \times 10^{10} s^{-1}$ using $\Gamma_{SO_2}^\infty = 4.3 \times 10^{15} molec \cdot cm^{-2}$

and $\Delta G_{gs} = -2.7 kcal/mol$ ($H_{cc}^{gs} = 100$). k_{solv} is then calculated from the mass accommodation

coefficient via $\alpha = \frac{k_{solv}}{(k_{des} + k_{solv})}$ giving $k_{solv}^{min} = 1.1 \times 10^6 s^{-1}$ using $\alpha = 0.110$ and

$k_{solv}^{max} = 7.1 \times 10^{12} s^{-1}$ using $\alpha = 0.175$. Finally, we calculate the rate of adsorption from the bulk

phase to the interface:

$$k_{desolv} = \frac{k_{solv} \cdot \delta}{H_{cc}^{sb} \cdot \Gamma_{SO_2}^{\infty}}, \quad (2)$$

where $H_{cc}^{sb} = \frac{H_{cc}^{gb}}{H_{cc}^{gs}}$. Thus, $k_{desolv}^{min} = 8.3 \times 10^{-15} \text{ cm}^3 \cdot \text{molec}^{-1} \cdot \text{s}^{-1}$ using $\Gamma_{SO_2}^{\infty} = 4.3 \times 10^{15} \text{ molec} \cdot \text{cm}^{-2}$ and $H_{cc}^{gs} = 8,400$ and $k_{desolv}^{max} = 6.6 \times 10^{-12} \text{ cm}^3 \cdot \text{molec}^{-1} \cdot \text{s}^{-1}$ using $\Gamma_{SO_2}^{\infty} = 4.0 \times 10^{14} \text{ molec} \cdot \text{cm}^{-2}$ and $H_{cc}^{gs} = 100$.

Table S2. Summary of Limiting Parameters Governing SO₂ Partitioning and Calculated Rate Coefficients.

Parameter	Minimum	Maximum
α	0.110	0.175
$\Gamma_{SO_2}^{\infty} (\text{molec} \cdot \text{cm}^{-2})$	4.0×10^{14}	4.3×10^{15}
$H_{cc}^{gs} = \exp\left(\frac{-\Delta G_{gs}}{RT}\right)$	100	8,400
${}^a k_{des} (\text{s}^{-1})$	9.3×10^6	3.4×10^{10}
$k_{solv} (\text{s}^{-1})$	1.1×10^6	7.1×10^9
${}^b k_{desolv} (\text{cm}^3 \cdot \text{molec}^{-1} \cdot \text{s}^{-1})$	8.3×10^{-15}	6.6×10^{-12}

${}^a k_{des}$ is inversely proportional to H_{cc}^{gs} , thus k_{des}^{min} is calculated using the maximum value of H_{cc}^{gs} and k_{des}^{max} is calculated using the minimum value of H_{cc}^{gs} .

${}^b k_{desolv}$ is inversely proportional to $\Gamma_{SO_2}^{\infty}$, thus k_{desolv}^{min} is calculated using the maximum value of $\Gamma_{SO_2}^{\infty}$ and k_{desolv}^{max} is calculated using the minimum value of $\Gamma_{SO_2}^{\infty}$.

Simulations run using the minimum and maximum values shown in Table S2 showed that the minimum values for SO₂ partitioning rate constants most closely replicated experimental data. These values are thus used in all simulations presented here. Hydrated SO₂ (SO₂·H₂O) also participates in coupled equilibria with sulfite and bisulfite with the net reaction:



where the rate constants are calculated by:

$$k_{fT} = \frac{K_{a1}K_{a2}k_{b2}}{[H^+]}s^{-1}; k_{bT} = \frac{k_{b1}[H^+]^2}{K_{a2}}s^{-1} \quad (S3)$$

See Deal, *et al.*¹ for the derivation of reaction RS1 and Equation S3.

S1.2. 2-Compartment and 3-Compartment Models

Typical kinetic simulations consist of two compartments (Figure S1A): a surface compartment with thickness of 1 nm and a bulk compartment with a thickness of $r/3$, or ~8500 nm for the experiments modeled here. When Kinetiscope models diffusion between these compartments, the probability of a molecule diffusing is proportional to the difference in concentration and to the distance between the midpoints of each compartment, or ~4000 nm for the experiments modeled here. When modeling 'bulk only' kinetics, this distance dramatically slows reaction kinetics making it appear that no thiosulfate decay occurs and when determining surface reaction fractions that can artificially enhance the number of reactions occurring at the interface. To circumvent these issues, we add a third 'reaction-diffusion compartment' (Figure S1B) with a compartment thickness corresponding to the reacto-diffusive length:

$$l = \sqrt{\frac{D_{O_3}}{k \cdot [S_2O_3^{2-}]}}$$

where D_{O_3} is the diffusion coefficient for ozone and k is the rate constant for the reaction between ozone and thiosulfate. Data recreated from Deal, *et al.*¹ were acquired with a bulk thiosulfate concentration of 0.25 M, resulting in $l \sim 10$ nm.

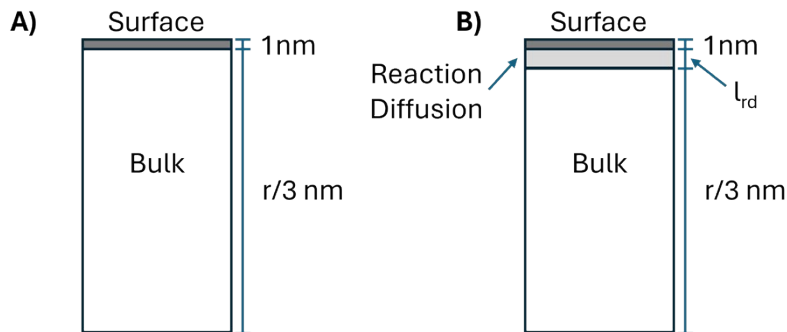


Figure S1. Schematics for the 2-compartment (A) and 3-compartment (B) kinetic models.

This method is only used in select cases as it is computationally expensive. Sensitivity checks were performed as shown in Section S1.3 to confirm that the two-compartment model is sufficient when modeling full droplet chemistry.

S1.3. Comparison Between Two-Compartment and Three-Compartment Models

Simulations at all three pH values were run using the two-compartment model (surface and bulk) and three-compartment model (surface, reaction-diffusion, and bulk), and results are shown in Figure S2. While there are some differences in results, we find that the two-compartment model adequately reproduces the experimental results given the range of equilibrium constants and surface concentrations of thiosulfate discussed in Section 3.1 of the main manuscript.

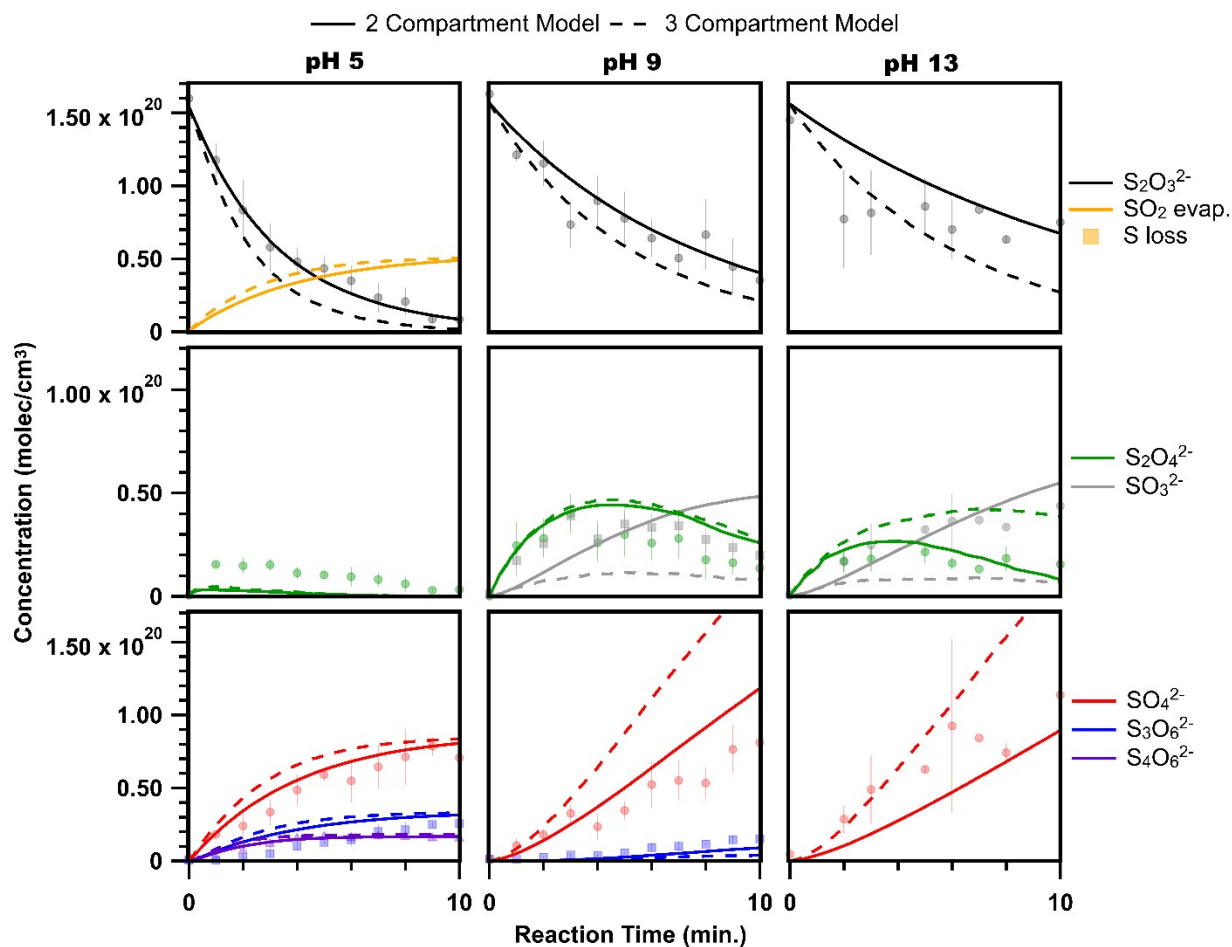


Figure S2. Results from simulations run with two compartments (surface and bulk) or three compartments (surface, reaction-diffusion, and bulk) compared to experimental data. Simulations run with the two-compartment model took 15 minutes to complete while simulations run with the three-compartment model took 24+ hours to complete.

S2. Liquid Flat Jet APXPS Measurements

Ambient pressure X-ray photoelectron spectroscopy (APXPS) is an excellent tool to provide insights into the interfacial chemical composition systems like atmospheric aerosols^{10, 24} due to the near ambient pressure conditions in the experimental chamber (up to a few millibar), which are in the pressure range of the stratosphere,²⁵ and the short effective attenuation length (EAL) of the excited electrons makes the technique surface sensitive. By changing the photon energy, and respectively the photoelectron kinetic energy, the EAL and the information depth of the measurement can be deliberately fine-tuned in the range of a few nm, allowing for depth profiling near the interface. Liquid jet systems have, in recent years, made the investigation of liquid/vapor interfaces more accessible.^{24, 26-28} One of the great advantages of liquid jet systems is the constant flow of liquid leading to a permanent interchange of the probed solution at the measurement position. Potential beam damage effects can thus be excluded from the measurements in this study. Liquid flat jet systems provide a nearly planar liquid surface.²⁶ The flat liquid sheet enhances, compared to the more common circular jet systems, the achievable electron intensities by a factor of $\pi/2$ (for a 90° incident beam compared to the electron detector direction), resulting in a better signal to noise ratio, optimal to study lower concentrated solutions.^{24, 28, 29}

S2.1. Experimental Methods

An aqueous 0.5 M sodium thiosulfate solution was prepared with sodium thiosulfate powder ($\text{Na}_2\text{S}_2\text{O}_3$, Sigma-Aldrich, ReagentPlus®, 99.0 %) solved in DI water. The APXPS measurements were conducted at the Advanced Light Source (ALS) at beamline 11.0.2.1 in the LARaXS endstation using a colliding micro liquid flat jet system described elsewhere.²⁹ In this setup the electric field vector of the linear polarized light is approximately at an angle of 35.3° with respect to the analyzer direction, which means that the influence of the anisotropy parameter (β) to the differential cross section is not negligible. The jet nozzles had an aperture diameter of 33 μm and the solution was supplied using a Knauer Blue Shadow 40P HPLC pump operated with a flow

rate of 3.8 mL/min and pressures around 65 bar. During all measurements, the pressure in the experimental chamber was in the low 10^{-4} Torr region, achieved with the help of a liquid nitrogen filled cooling trap, but the pressure was likely higher in the proximity of the liquid flat sheet.

A survey spectrum of the 0.5 M sodium thiosulfate ($\text{Na}_2\text{S}_2\text{O}_3$) solution measured with an excitation energy of 900 eV is shown in Figure S3. All expected core level peaks and the O KLL Auger peak related to water and sodium thiosulfate are present. The S 2s and S 2p core level show the two different sulfur components of $\text{Na}_2\text{S}_2\text{O}_3$, related to sulfur with different oxidation states.

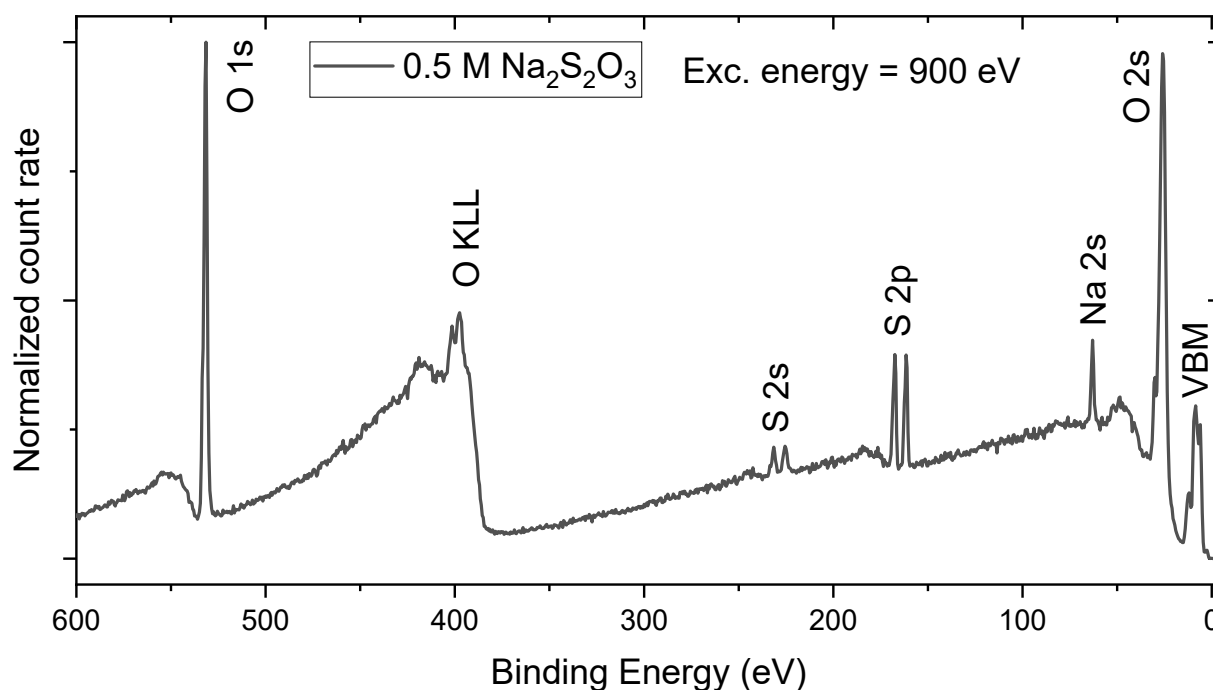


Figure S3. Survey spectra of the 0.5 M sodium thiosulfate ($\text{Na}_2\text{S}_2\text{O}_3$) solution measured with an excitation energy of 900 eV. The water and sodium thiosulfate core levels, the O KLL Auger peak and the valence band maximum (VBM) are labelled.

S2.2. O 1s Core Level Fits

The O 1s core level spectra, shown in Figure S4, are measured with different excitation energies, which result in different excess kinetic energies and an increasing EAL. Excitation energies were varied to produce electrons with excess kinetic energies of 100 eV, 215 eV, 250

eV, 300 eV, 350 eV, 400 eV, 450 eV, 500 eV, 550 eV, 600 eV, 700 eV, and 800 eV. Peak areas were determined by fitting three Voigt functions and a linear background function for each spectrum using the program fityk 0.9.3³⁰. The three Voigt functions account for the main peak around 536.9 eV, corresponding to water in the liquid phase (O(l)), a peak around 538.7 eV, corresponding to water in the gas phase (O(g)) and a small peak around 535.1 eV for the thiosulfate ($\text{S}_2\text{O}_3^{2-}$) component. The $\text{S}_2\text{O}_3^{2-}$ component is additionally shown as an inset in each spectrum to increase visibility.

The Lorentzian FWHM of all Voigt functions was restricted to be the same in every spectrum and the fit delivered a value of 0.18 eV, close to the literature value of core-hole lifetime calculations of 0.1 eV.³¹ The Gaussian FWHM reflecting the experimental broadening was allowed to be different for each excitation energy and for the peak accounting for the water gas phase, but it was restricted to be the same for the liquid water and the $\text{S}_2\text{O}_3^{2-}$ peak for each excitation energy. Furthermore, the distance between the $\text{S}_2\text{O}_3^{2-}$ peak and the liquid water peak was restricted to be the same in each spectrum and the fit delivered 1.76 eV. The binding energy of all peaks have been corrected by measurements of the valence band and shifting the water gas phase orbital ($1b_1(g)$) to a binding energy of 12.60 eV.

Due to the energy dependence of the EAL, each kinetic energy corresponds to a different information depth into the solution, increasing with the electron kinetic energy. Using data for pure water as an estimate, the 100 eV kinetic energy spectrum corresponds to an EAL of ~1.5 nm and the 800 eV kinetic energy spectra corresponds to an EAL of 5 nm.³² The increased surface sensitivity of the APXPS measurements towards lower electron kinetic energies is nicely visible in Figure S4 by the relative increase of the water gas phase peak.

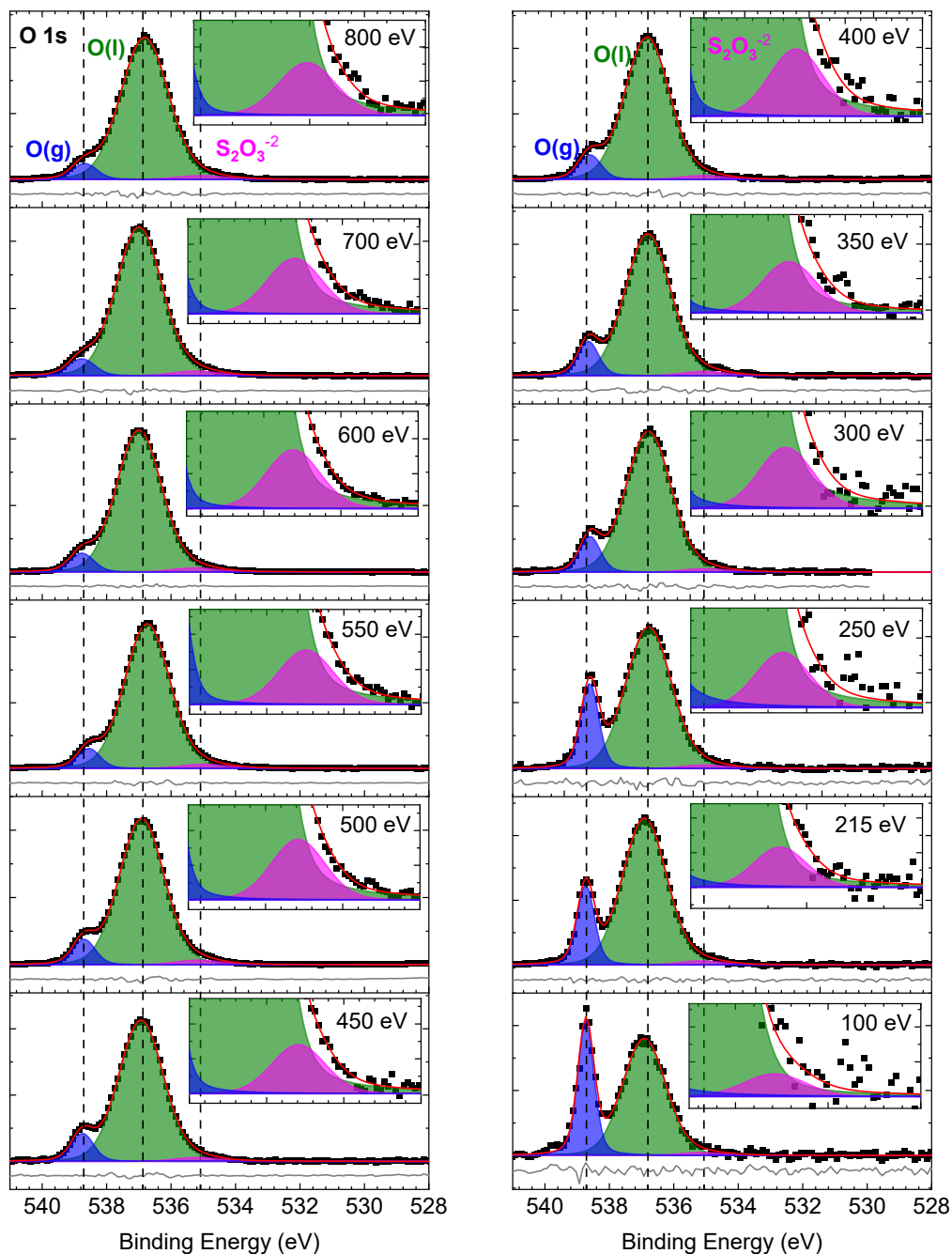


Figure S4. The O 1s spectra of the prepared 0.5 M aqueous sodium thiosulfate solution recorded with different excitation energies resulting in electrons with kinetic energies of 100 eV, 215 eV, 250 eV, 300 eV, 350 eV, 400 eV, 450 eV, 500 eV, 550 eV, 600 eV, 700 eV, and 800 eV. The three peaks correspond to the liquid (green, O(l)) and gas water (blue, O(g)) and thiosulfate (magenta, $S_2O_3^{2-}$) components.

S2.3. Thiosulfate ($\text{S}_2\text{O}_3^{2-}$) surface concentration

Derived O 1s peak areas can be used to calculate the $\text{S}_2\text{O}_3^{2-}$ molar concentration. The corrected $\text{S}_2\text{O}_3^{2-}$ peak area was divided by the corrected liquid water peak area, divided by three to account for stoichiometry, and multiplied by the concentration of water (55.5 M). The liquid water peak areas are corrected by the O 1s differential cross section accounting for the anisotropy parameter (β) for liquid water derived by Thürmer et al., ~ 1.5 in the energy range used here.³² The $\text{S}_2\text{O}_3^{2-}$ peak areas were corrected with the O 1s differential cross section values of Trzhaskovskaya et al. calculated with the quadrupole approximation with β close to 2.^{33, 34} Whether the differential cross section values derived for elements in the gas phase are correct for solvated ions like thiosulfate is debatable,^{28, 35} but, to our knowledge, β values for thiosulfate in the O 1s core level are not available in the literature. Both peaks were measured with the same excitation energy, thus photon flux and detector transmission function corrections are not required.

The calculated thiosulfate concentration is shown in Figure S5A as a function of photoelectron kinetic energy. From left to right the information depth, i.e. the EAL of the results, increases from roughly 1.5 nm to 5 nm,³² meaning that the most surface sensitive measurement is presented at the far left. Given that the signal comes from electrons originating from the region confined by the interface and the EAL, the noted depths should be considered the maximum penetration depth. The measured thiosulfate concentration, with the uncertainty derived from the fit, is consistent with the 0.5 M concentration of the prepared solution represented by the dashed line. Towards the lower kinetic energy measurement, i.e. the more surface sensitive measurement, the average thiosulfate concentration slightly decreases, but uncertainty still encompasses the 0.5 M concentration. The increased uncertainty of concentration is due to the decreased signal to noise ratio of the spectra, resulting in a larger uncertainty of the peak areas derived from the fit. Overall, the surface concentration of thiosulfate appears approximately equal to the bulk concentration of

0.5 M with the most surface sensitive measurement giving $[S_2O_3^{2-}]_{(ads)}^{b=0.5 M} = 0.4 \pm 0.2$ M. Note

that this is a different value than that used for kinetic modeling, $[S_2O_3^{2-}]_{(ads)}^{b=0.25 M}$.

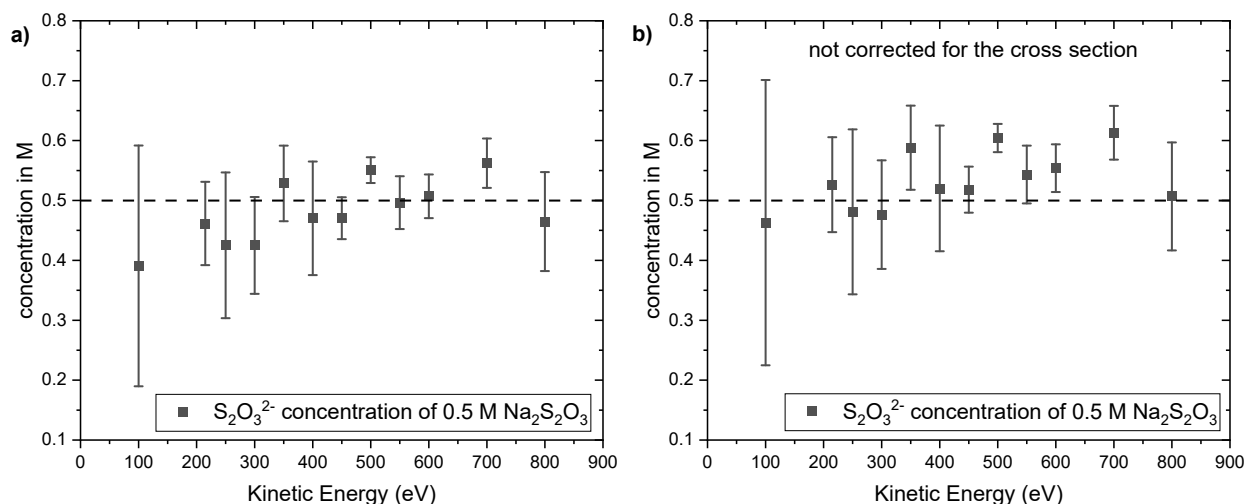


Figure S5. a) The molar $S_2O_3^{2-}$ concentration calculated for each kinetic energy as explained in the text. The dashed black line indicates the molar concentration of the prepared 0.5 M aqueous sodium thiosulfate solution. b) the molar $S_2O_3^{2-}$ concentration calculated without a cross-section correction.

To show the influence of the used different cross section, values, we calculated the molar thiosulfate concentration without the cross-section correction shown in Figure S5. This calculation assumes that the differential cross section and anisotropy parameter of liquid water and solvated thiosulfate are similar. The impact on the results is small, leading to ~ 0.05 M higher thiosulfate concentrations, and the main result, that the measured molar thiosulfate concentration agrees with the concentration of the prepared 0.5 M solution, is still valid. Combining the results of both approaches shown in Figure S5A,B, we constrain the thiosulfate concentration of our most surface sensitive measurement as between 0.2 and 0.6 M.

S3. Constraining $[S_2O_3^{2-}]_{(ads)max}$ Using DUV-SHG and APXPS Experiments

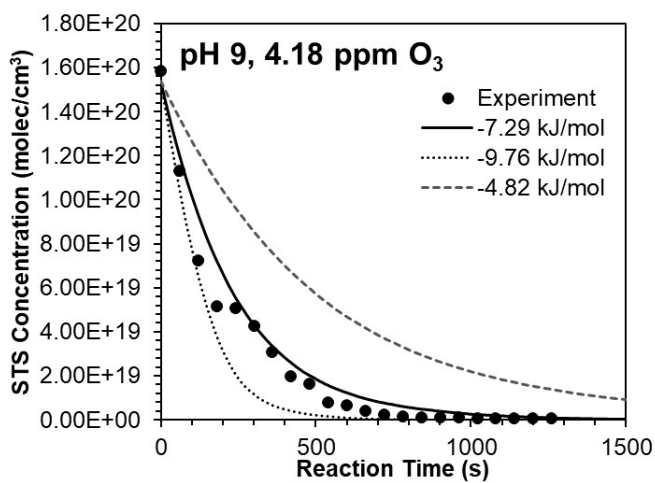
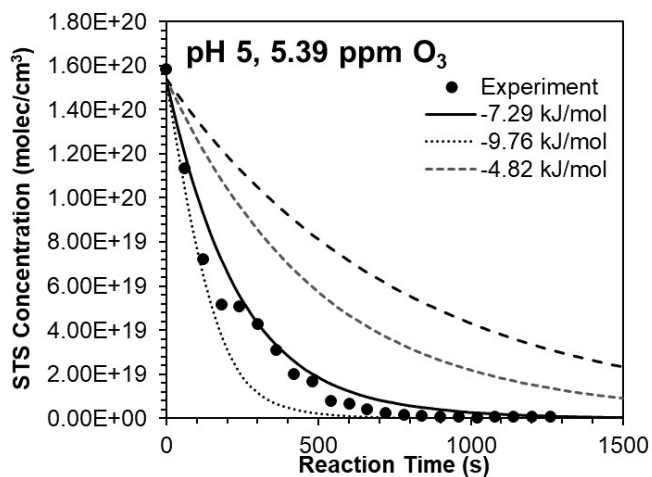
Given the uncertainty in the surface concentration of thiosulfate (0.2 to 0.6 M) measured with APXPS for a thiosulfate solution with a bulk concentration of 0.5 M (Section S2.3) we examine a range of values for the maximum concentration for adsorbed thiosulfate, $[S_2O_3^{2-}]_{(ads)max}$. First, the equilibrium constant for adsorption, K_{eq}^{ads} , is calculated by $K_{eq}^{ads} = \exp\left(\frac{\Delta G_{ads}}{RT}\right) * C_W$, where C_W is the concentration of water (55.5 M), R is the universal gas constant, and $T = 298K$. We note that there is also some uncertainty in the Gibbs free energy for adsorption for thiosulfate, $\Delta G_{ads}^{S_2O_3^{2-}} = -7.3 \pm 2.5 kJ/mol$, measured in DUV-SHG experiments (Section 3.1 in the main text). For simplicity, we use the average value (-7.3 kJ/mol), resulting in $K_{eq}^{ads} = 19$. $[S_2O_3^{2-}]_{(ads)max}$ is then calculated by rearranging the Langmuir equation:

$$[S_2O_3^{2-}]_{(ads)max} = [S_2O_3^{2-}]_{(ads)}^{b=0.5 M} \left/ \frac{K_{eq}^{ads} \cdot 0.5 M}{1 + K_{eq}^{ads} \cdot 0.5 M} \right., \quad (4)$$

where $[water_{(b)}] = 55.5 M$ and $[S_2O_3^{2-}]_{(ads)}^{b=0.5 M}$ is the average value measured by APXPS (0.4 M), the average value minus one standard deviation (0.2 M), or the average value plus one standard deviation (0.6 M). This results in $[S_2O_3^{2-}]_{(ads)max} = 1.3 M, 2.7 M,$ and $4.0 M$. Note that although $[S_2O_3^{2-}]_{(ads)max}$ should only have 1 significant figure, two are used here to avoid confusion due to rounding.

As shown in Figure S6, Deal, *et al.*¹ found that $\Delta G_{ads}^{S_2O_3^{2-}} = -7.3 kJ/mol$ most closely represents thiosulfate decay at pH 5 and pH 9 and $\Delta G_{ads}^{S_2O_3^{2-}} = -4.8 kJ/mol$ most closely represents thiosulfate decay at pH 13. Thus, $[S_2O_3^{2-}]_{(ads)max}$ values are benchmarked to experimental data using two sets of kinetic simulations with $\Delta G_{ads}^{S_2O_3^{2-}} = -7.3 kJ/mol$ (Figure S7) and

$\Delta G_{ads}^{S_2O_3^{2-}} = -4.8 \text{ kJ/mol}$ (shown in Figure 3 in the main text). The results are discussed in Section 3.1 of the main text.



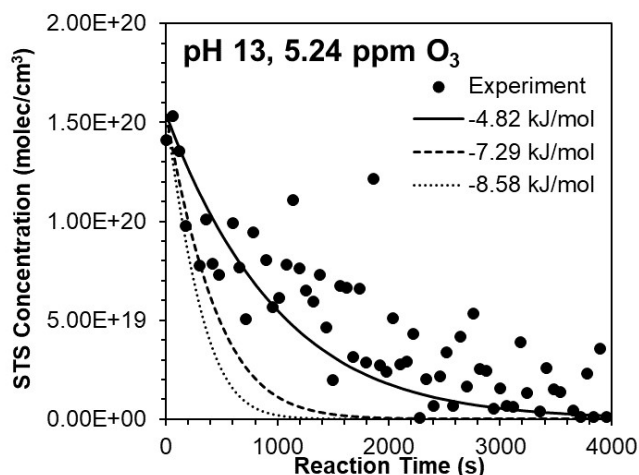


Figure S6. Model (lines) comparison to experimental data (points) as a function of ΔG_{ads} at each pH. Recreated with permission from Deal, *et al.*¹ Copyright 2024 American Chemical Society.

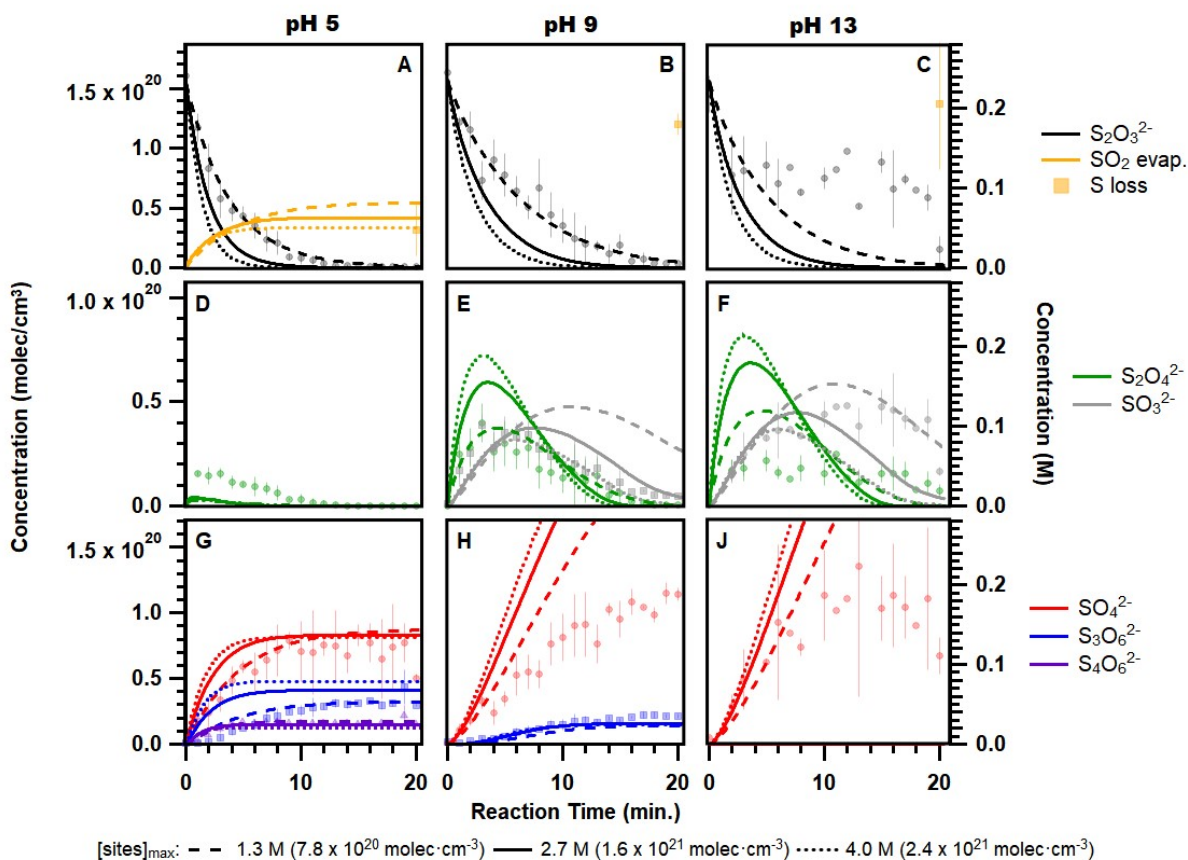


Figure S7. Representative reaction kinetics for the ozone oxidation of thiosulfate ($\text{S}_2\text{O}_3^{2-}$) in pH 5 (A,D,G), pH 9 (B,E,H), and pH 13 (C,F,J) solutions compared with simulation results using $\Delta G = -7.3$ kJ/mol and three values for the maximum concentration of adsorbed thiosulfate (values shown in legend). Experimental data (points) are recreated from Deal, *et al.*¹ with error bars representing one standard deviation in a set of 5 repeats.

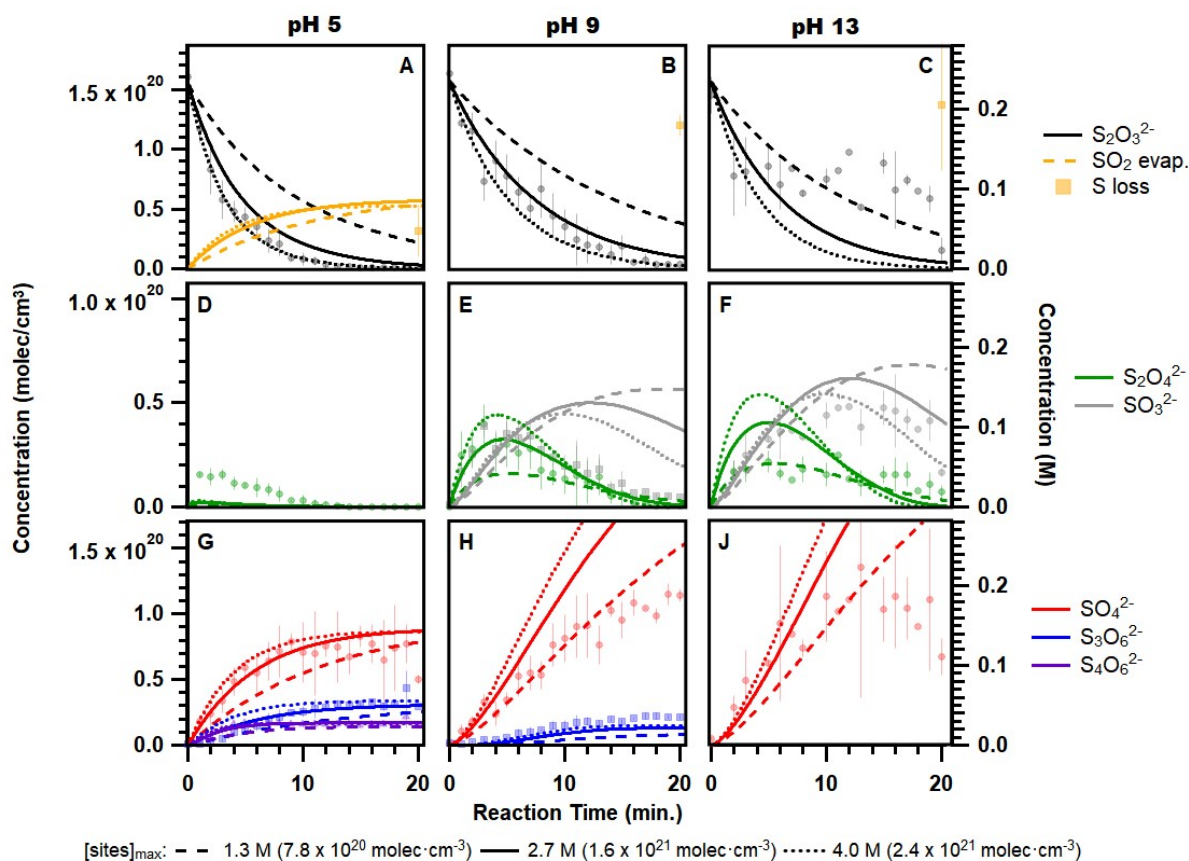


Figure S8. Representative reaction kinetics for the ozone oxidation of thiosulfate ($S_2O_3^{2-}$) in pH 5 (A,D,G), pH 9 (B,E,H), and pH 13 (C,F,J) solutions compared with simulation results using $\Delta G = -4.8$ kJ/mol and three values for the maximum concentration of adsorbed thiosulfate (values shown in legend). Experimental data (points) are recreated from Deal, *et al.*¹ with error bars representing one standard deviation in a set of 5 repeats. Also shown as Figure 3 in the main text.

As stated in the main text, we find that the $\Delta G_{\text{ads}} = -7.3$ kJ/mol simulations only recreate experimental data at pH 5 and pH 9 (Figure S7), while the $\Delta G_{\text{ads}} = -4.8$ kJ/mol simulations with varying $[S_2O_3^{2-}]_{\text{max}}$ recreate the experimental data at all three pH values (Figure S8). Specifically, the simulated thiosulfate decay (Figure S8A,B,C black), trithionate production (Figure S8G,H blue), and tetrathionate production (Figure S8G purple) show excellent agreement with experimental data. The simulated sulfate production (red) also shows excellent agreement with experimental data at pH 5 (Figure S8G) but overestimates the amount of observed sulfate production at pH 9 (Figure S8H). This discrepancy at pH 9 is likely due to the high sulfur loss (Fig.

S8B, orange point), which the kinetic model does not account for. Comparing the simulated and experimental results for dithionite and sulfite is more complicated due to uncertainties in the concentrations for each of these species. Dithionite is not stable in aqueous solution, where it decomposes into sulfite and sulfate,³⁶ meaning that calibration curves were not obtained for dithionite and the concentrations shown here are qualitative rather than quantitative. Furthermore, because dithionite decomposes into sulfite, the experimental sulfite signal at pH 9 (Figure S8E grey) may be skewed. Despite these issues, we find that the kinetic simulations do accurately replicate the kinetic behavior of dithionite (Figure S8D,E,F green).

We note that although OH^- is known to react with ozone, which could also explain the reduced thiosulfate decay observed at pH 13, the rate constant ($< 100 \text{ M}^{-1} \text{ s}^{-1}$ or $< 2 \times 10^{-19} \text{ cm}^3 \text{ molec}^{-1} \text{ s}^{-1}$)³⁷ is ~6 orders of magnitude smaller than the rate constant for the reaction of thiosulfate with ozone ($7.2 \times 10^7 \text{ M}^{-1} \text{ s}^{-1}$ or $1.20 \times 10^{-13} \text{ cm}^3 \text{ molec}^{-1} \text{ s}^{-1}$).^{3, 38} This means that almost all of the thiosulfate has to be depleted before the $\text{OH}^- + \text{O}_3$ reaction becomes competitive. Given that we still detect significant amounts of thiosulfate at long reaction times, we consider $\text{OH}^- + \text{O}_3$ as a negligible contributor to the reaction kinetics. We also note that although we model the pH as the same in the bulk and surface compartments, there is some evidence for enhanced acidity near the interface.³⁹ While it is possible our modeling of pH is too simplistic, enhanced acidity at the interface likely does not explain the pH 13 kinetics as we would expect to see formation of trithionate or tetrathionate. On the other hand, there is some evidence that anion reactions with ozone are slower at the interface in highly alkaline environments.²

S4. DUV-SHG of Thiosulfate at pH 13

Additional DUV-SHG measurements of thiosulfate solutions adjusted to pH 13 were performed to uncover potential changes in the interfacial response. A suppression of thiosulfate ions at the interface would manifest as decreased SHG intensity and may exhibit a non-Langmuir response. Figure S9 displays the normalized SHG response of thiosulfate at pH 13 and at first glance the extracted ΔG_{ads} of thiosulfate appears to shift in agreement with the kinetic model. However, the uncertainty in these measurements remains large and the intensity of the SHG response is not significantly different than the pH 6 measurements. Why then does the alkaline environment data predict a less favorable free energy? Analyzing the data in Figure S9 closer, we find that the high concentration points significantly affect the value of the extracted free energy. This observation is highlighted in Figure S9B where we track the ΔG_{ads} as more points are included in the fit. Previous SHG studies observed increased SHG signal at high concentrations that was not well fit using a Langmuir model.⁴⁰ This response was attributed to ion pairing effects that become more prominent with increased solute concentration. The SHG response appears to shift away from a Langmuir shape and may be indicative of unfavorable ion-pairing contributions.

Additionally, studies indicate that hydroxide ions are repelled from the air-water interface and accumulate in a subsurface layer.¹² It is unclear how this accumulated hydroxide layer may interact with co-solvated ions such as thiosulfate. Seki et al. saw an increased surface activity (< 50%) in hydrophobic ions with the addition of co-solvated hydrophilic ions.⁷ Their work finds the addition of hydrophilic ions affects ion speciation across the interfacial landscape. This reasoning does not explain why the magnitude of the SHG response remains similar for pH 13 solutions since we would then expect a greater response from thiosulfate. Thus, while our data suggests that the ΔG_{ads} of thiosulfate at the air-water interface is less favorable with increased pH, we do not have the complete molecular details to explain this effect.

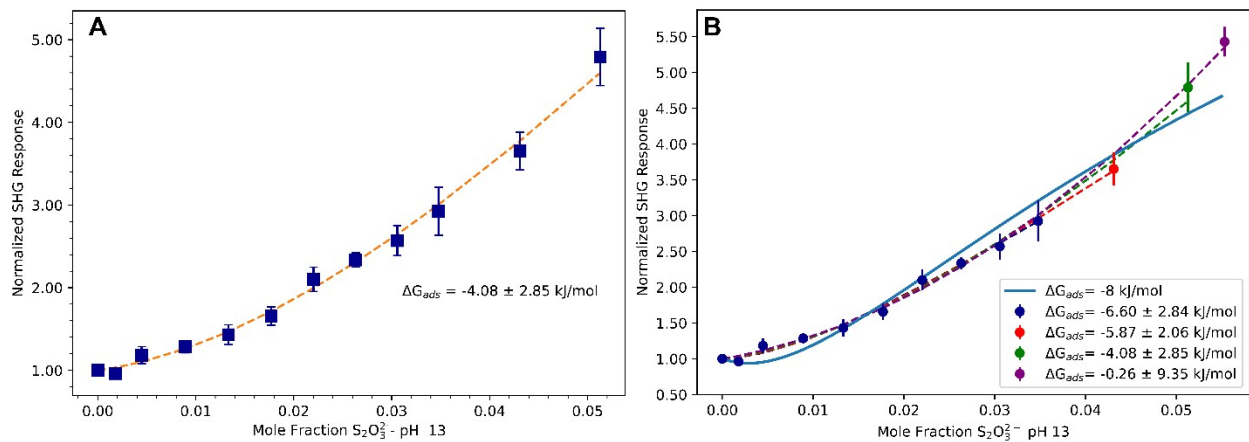


Figure S9. Normalized DUV-SHG response of sodium thiosulfate solutions at pH 13. A) DUV-SHG response of thiosulfate fit to a Langmuir model exhibiting a less favorable ΔG_{ads} . B) The extracted ΔG_{ads} is recorded as high concentration points are included in the fit. For reference, a fixed ΔG_{ads} Langmuir fit is provided (solid blue line).

S5. Agreement Between Experimental Data and Kinetic Model Predictions

As shown by the dashed lines Figure S10D,E,F, restricting chemistry to the surface does not accurately capture the decay kinetics for dithionite ($S_2O_4^{2-}$, green) and results in negligible sulfite (SO_3^{2-} , grey) formation. Note that although experimental results cannot distinguish between $S_2O_4^{2-}$ and its conjugate acid, $HS_2O_4^-$, simulations suggest that $[S_2O_4^{2-}] \gg [HS_2O_4^-]$ at all pH values studied here. In Figure S10G,H,J, we see that restricting chemistry to the surface compartment produces a negligible amount of the expected final products in pH 9 and pH 13 solutions (Figure S10H,J), and no tetrathionate ($S_4O_6^{2-}$, purple) and too much trithionate ($S_3O_6^{2-}$, blue) in the pH 5 solution (Figure S10G). On the other hand, restricting chemistry to the bulk compartment shows reasonable agreement with dithionite ($S_2O_4^{2-}$, green) kinetics (Figure S10D,E,F) and reasonable agreement with the final concentrations of final products at pH 5 (Figure S10G) but does not accurately capture the maximum dithionite concentration at pH 9 (Figure S10E), final product kinetics at early times at pH 5 (Figure S10G), or trithionate ($S_3O_6^{2-}$, blue) production at pH 9 (Figure S10H). This suggests that the ozonation of thiosulfate in droplets formed from pH 5 and pH 9 solutions relies on *both* surface and bulk chemistry.

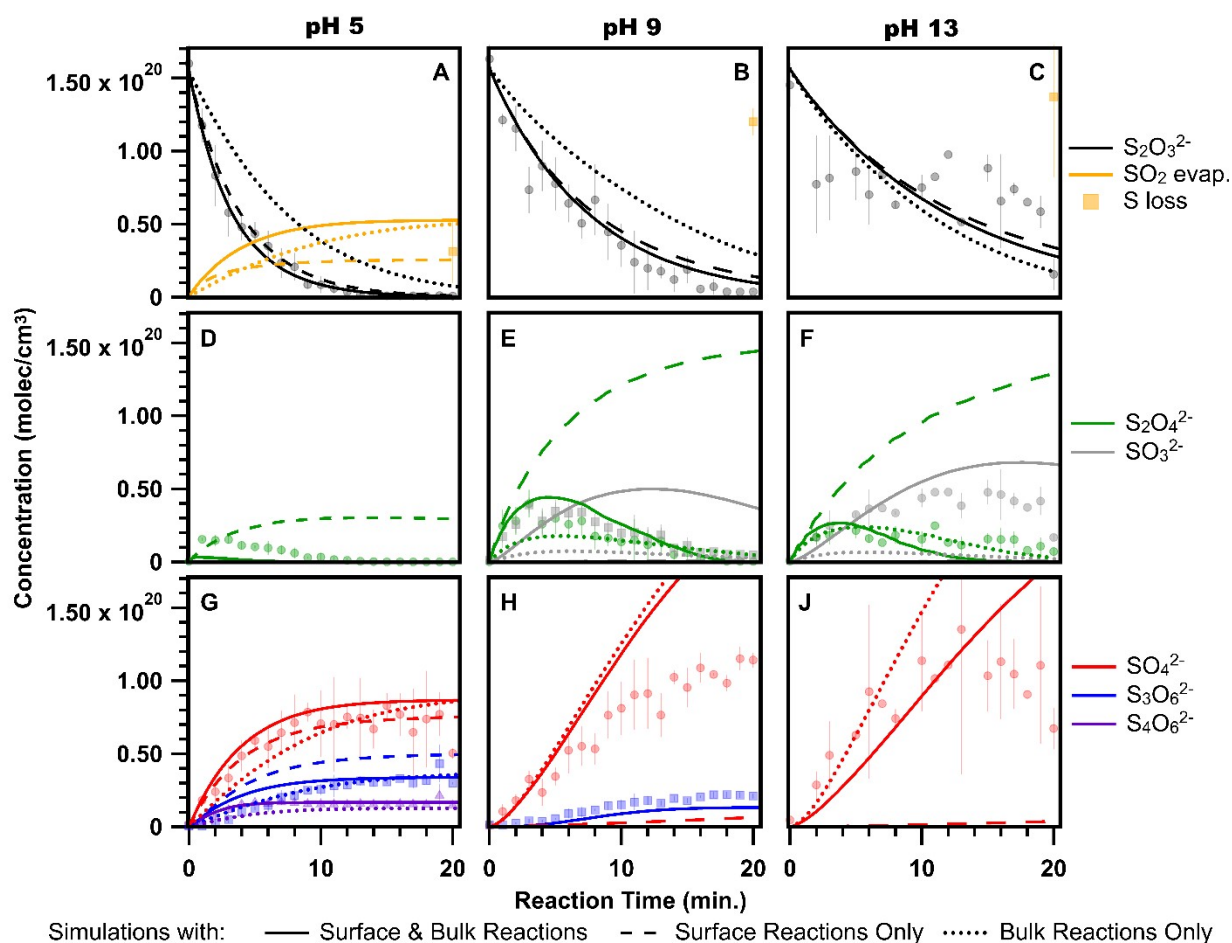


Figure S10. Contributions from surface and bulk chemistry to the ozone oxidation of thiosulfate ($S_2O_3^{2-}$) in pH 5 (A,D,G), pH 9 (B,E,H), and pH 13 (C,F,J) solutions. Experimental data (points) are recreated from Deal, *et al.*¹ with error bars representing the standard deviation in a set of 5 repeats. Simulation results include both surface and bulk reactions (solid lines), only surface reactions (dashed lines), or only bulk reactions (dotted lines).

Table S3. Agreement Between Experimental Data and Kinetic Model Predictions

Species	Kinetic Role	Surface Rxns Only	Bulk Rxns Only	Full Model
Thiosulfate ($S_2O_3^{2-}$; black)	Reactant	Good	Fair; too slow	Good
Dithionite ($S_2O_4^{2-}$; green)	Intermediate	Poor; does not capture decay kinetics	Fair; good kinetic agreement, does not always capture maximum concentration	Fair; good kinetic agreement, does not always capture maximum concentration
Sulfite (SO_3^{2-} ; grey)	Intermediate	Poor; predicts negligible production	Poor; predicts minimal production	Fair; good kinetic agreement, does not always capture maximum concentration

Sulfate (SO ₄ ²⁻ ; red)	Final product	Poor; good agreement at pH 5, predicts negligible production at pH 9 and 13	Fair; good kinetic agreement at long times, does not capture kinetics at early times and overpredicts concentrations at pH 9 and 13	Fair; good kinetic agreement, overpredicts concentrations at pH 9 and 13
Trithionate (S ₃ O ₆ ²⁻ ; blue)	Final product	Poor; overpredicts at pH 5, predicts negligible production at pH 9	Fair; good agreement for pH 5, predicts negligible production at pH 9	Fair; good agreement for pH 9, does not capture kinetics at early times for pH 5
Tetrathionate (S ₄ O ₆ ²⁻ ; purple)	Final product	Poor; predicts negligible production	Fair; does not capture kinetics at early times	Good

S6. Comparison Between Modeled Kinetics and All Data Reported by Hsu, *et al.*⁴¹

All experimental data in this section was recreated from Hsu, *et al.*⁴¹ and simulations were run using the same kinetic model described in the main manuscript and in Section S1. We note that our model deviates from the Hsu, *et al.*⁴¹ data for ozone concentrations <0.5 ppm (Experiments 6-9). Given the large error bars for these experimental data sets and extremely slow thiosulfate decay it is possible that there are ozone sinks in the experiments that are unaccounted for. Alternatively, it is possible there are missing steps in our reaction mechanism, but it is difficult to determine what this might be given the agreement with other portions of the data set such as experiments 4, 14, 15. Taking the data set as a whole, we find reasonable to fair agreement between our simulation results and the Hsu, *et al.*⁴¹ experimental data.

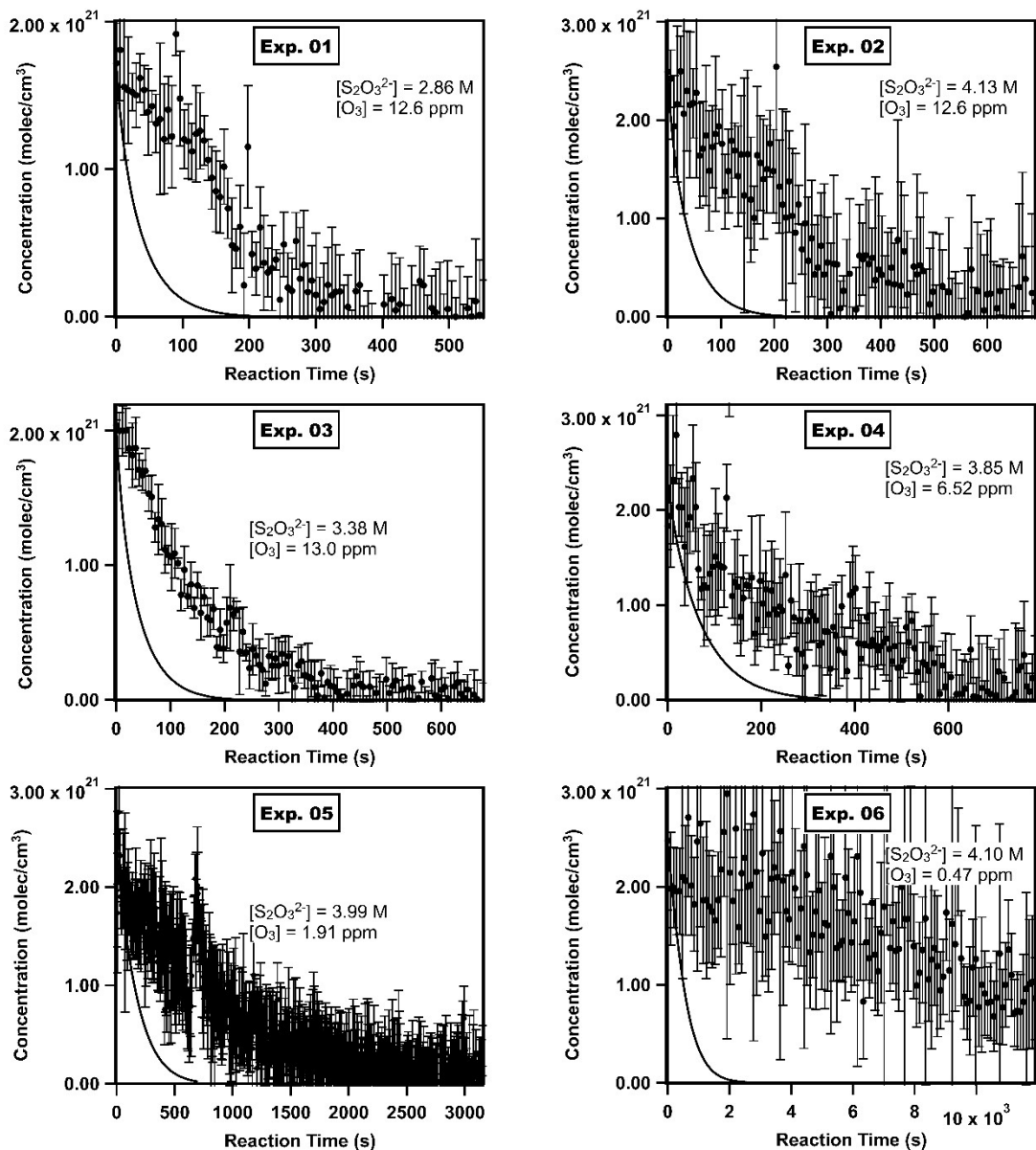


Figure S11. Comparisons between the kinetic model from this paper (lines) and data from *Hsu, et al.*⁴¹ (points, experiments 1-6). The concentration of thiosulfate and gas-phase ozone are shown in the figures. All droplets were $\sim 3 \mu\text{m}$ in radius.

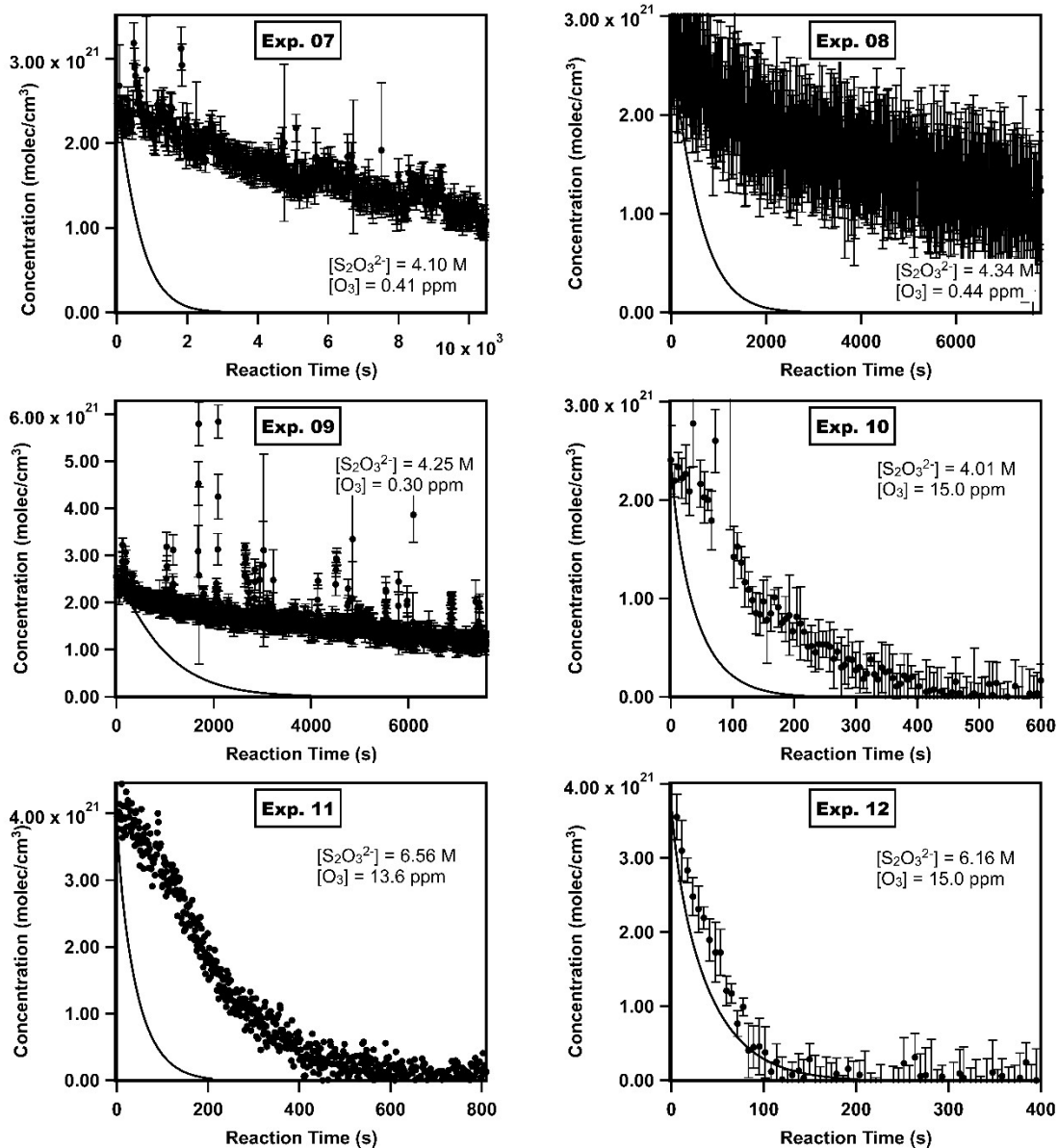


Figure S12. Comparisons between the kinetic model from this paper (lines) and data from Hsu, *et al.*⁴¹ (points, experiments 7-12). The concentration of thiosulfate and gas-phase ozone are shown in the figures. All droplets were $\sim 3 \mu\text{m}$ in radius.

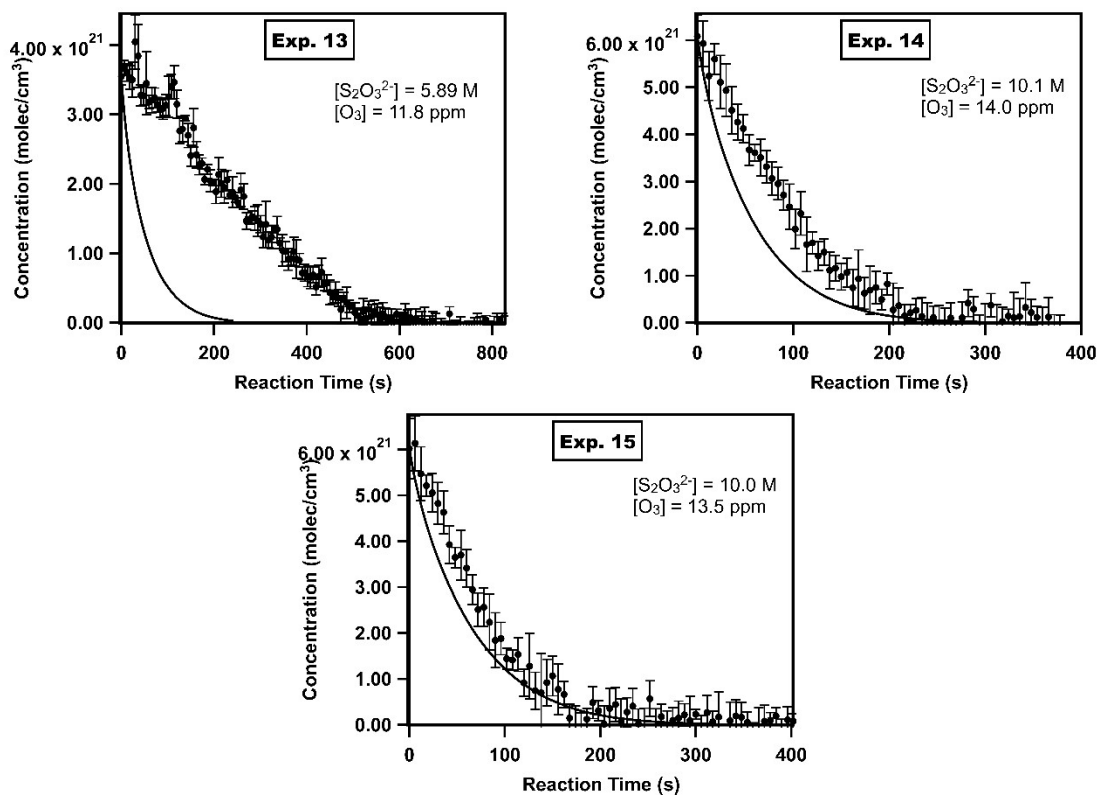


Figure S13. Comparisons between the kinetic model from this paper (lines) and data from Hsu, *et al.*⁴¹ (points, experiments 13-15). The concentration of thiosulfate and gas-phase ozone are shown in the figures. All droplets were $\sim 3 \mu\text{m}$ in radius.

S7. Levitated Droplets Experimental Schematic

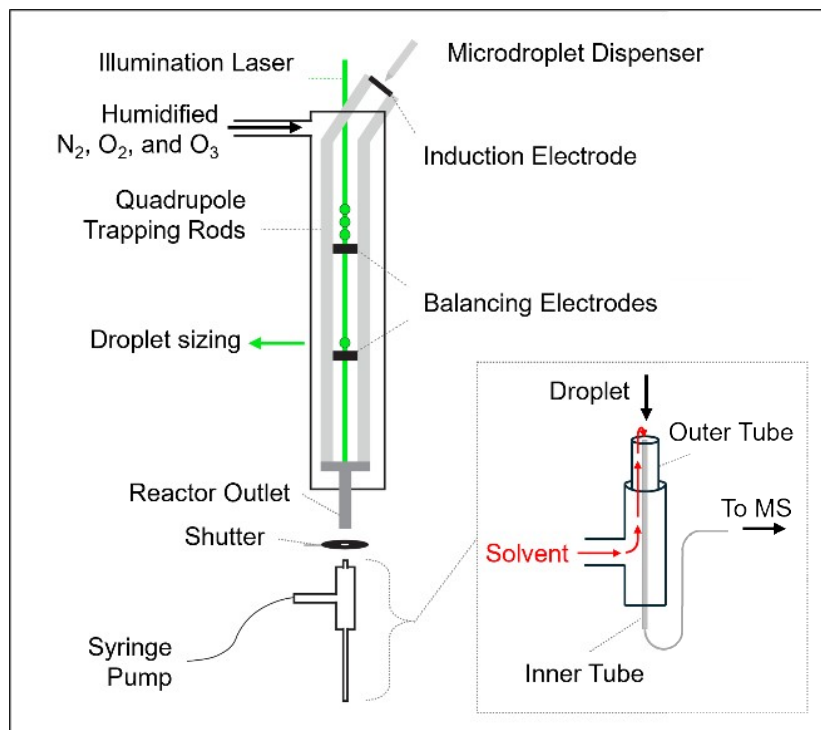


Figure S14. Experimental schematic of the quadrupole electrodynamic trap (QET) and (inset) the open-port sampling interface (OPSI) to the mass spectrometer. Adapted with permission from Deal, *et al.*¹ Copyright 2024 American Chemical Society.

S8. Calculated Ozone Concentration Near the Interface

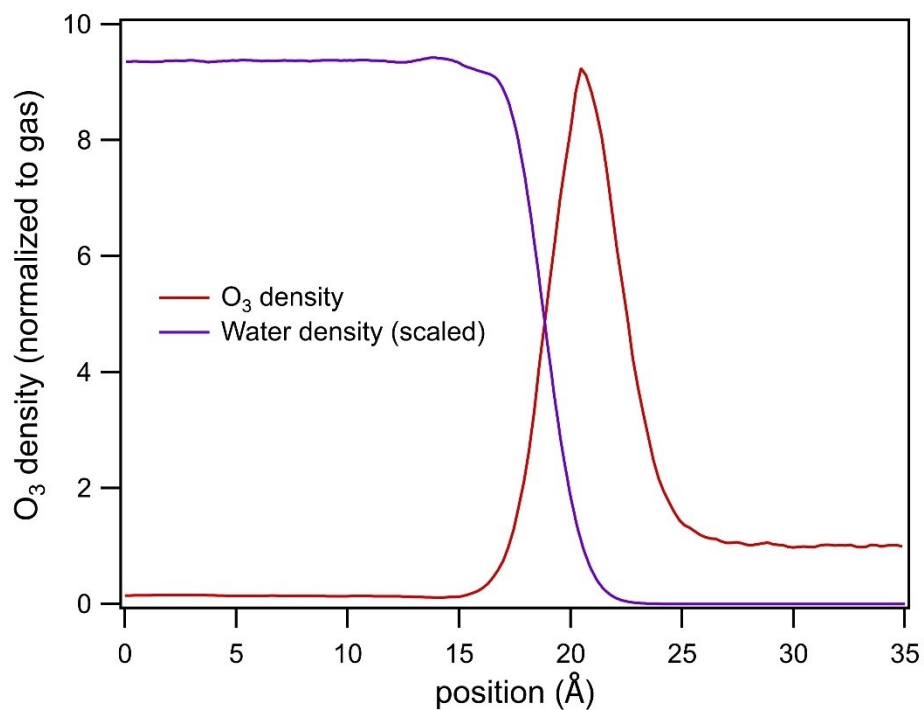


Figure S15. Calculated density of ozone (red) and water (purple) at the air-water interface. Recreated with permission from Prophet, *et al.*⁴² Copyright 2024 American Chemical Society.

S9. 3-Compartment Model Comparisons for Figure 7

See Section S1.2. for descriptions of the 2- and 3- compartment models and see Section S1.3. for a general comparison between 2-compartment and 3-compartment models. In Figure S16, we show select examples from Figure 7 in the main text run with a 3-compartment model to ensure that the overall trends in product yields and surface reaction probabilities are not affected by the 2-compartment approximation. The size of the reaction-diffusion compartment is set to reflect the reacto-diffusive length as calculated by Equation 16 in the main text. We see that the percent yield for each of the products calculated by the 3-compartment model (Figure S16A,B) is not significantly different than the percent yield for each of the products calculated by the 2-compartment model (Figure 7A,B in the main text). We note that all the % surface reaction values calculated by the 3-compartment model (Figure S16C,D) are lower than the % surface reaction values calculated by the 2-compartment model (Figure 7C,D in the main text). However, the general trends with changes in r , $[O_3]_{(gas)}$, and $[S_2O_3^{2-}]_0$ remain consistent with the conclusions gleaned in the main text.

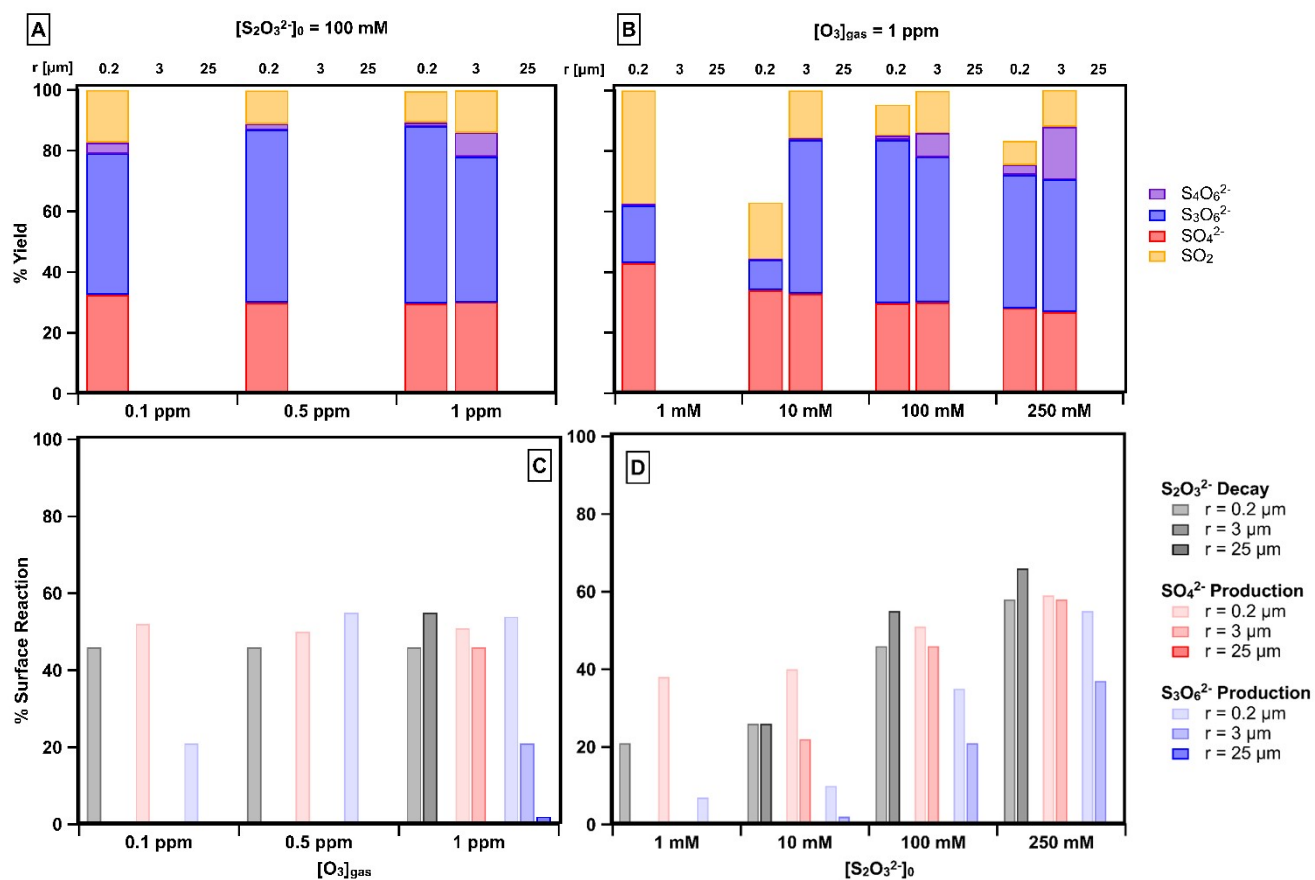


Figure S16. Select 3-compartment model results for product distributions (A,B) and proportion of reactions occurring at the droplet surface (C,D) for a range of gas-phase ozone concentrations ($[O_3]_{\text{gas}}$), initial bulk thiosulfate concentrations ($[S_2O_3^{2-}]_0$), and droplet radii. Data not shown was not calculated with the 3-compartment model due to extensive computation time.

S10. Average Sulfur Oxidation States for a Range of Droplet Sizes and Concentrations

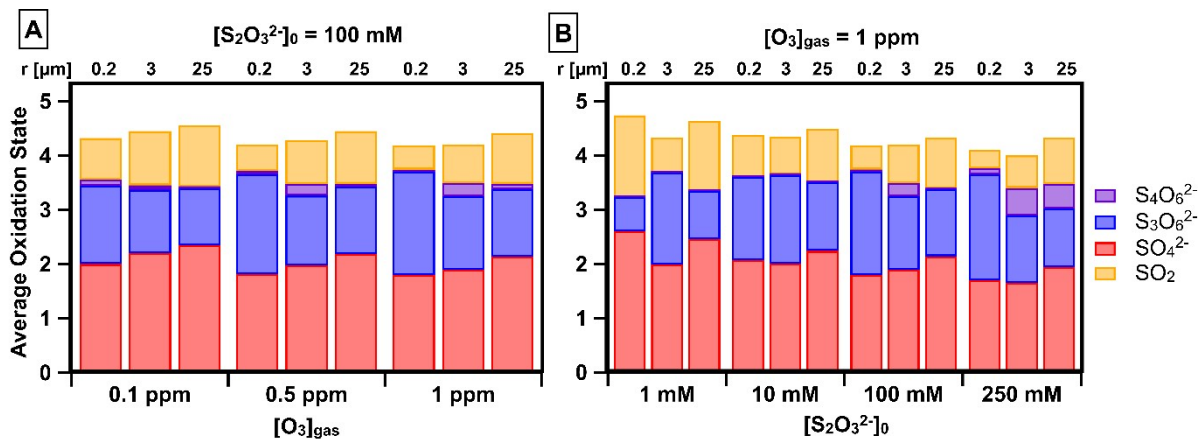


Figure S17. Average sulfur oxidation state for a range of gas-phase ozone concentrations, $[\text{O}_3]_{\text{gas}}$, (A), initial bulk thiosulfate concentrations ($[\text{S}_2\text{O}_3^{2-}]_0$), (B) and droplet radii (indicated across the top of each panel). Note: The average oxidation state is broken down into contributions from each product. Contributions from SO_4^{2-} , $\text{S}_3\text{O}_6^{2-}$, $\text{S}_4\text{O}_6^{2-}$, and SO_2 are indicated by red, blue, purple, and orange, respectively.

References

1. A. M. Deal, A. M. Prophet, F. Bernal, R. J. Saykally and K. R. Wilson, A detailed reaction mechanism for thiosulfate oxidation by ozone in aqueous environments, *Environ. Sci. Technol.*, 2024.
2. A. M. Prophet, K. Polley, G. J. Van Berkel, D. T. Limmer and K. R. Wilson, Iodide oxidation by ozone at the surface of aqueous microdroplets, *Chem. Sci.*, 2024, **15**, 736-756.
3. J. R. Kanofsky and P. D. Sima, Reactive absorption of ozone by aqueous biomolecule solutions: implications for the role of sulfhydryl compounds as targets for ozone, *Arch. Biochem. Biophys.*, 1995, **316**, 52-62.
4. M. Wayman and W. Lem, Decomposition of aqueous dithionite. Part II. A reaction mechanism for the decomposition of aqueous sodium dithionite, *Can. J. Chem.*, 1970, **48**, 782-787.
5. R. G. Rinker, T. P. Gordon, D. M. Mason, R. R. Sakaida and W. H. Corcoran, Kinetics and mechanism of the air oxidation of the dithionite ion ($S_2O_4^{2-}$) in aqueous solution, *J. Phys. Chem.*, 1960, **64**, 573-581.
6. G. Barker and D. Sammon, Kinetics of proton-transfer reactions, *Nature*, 1967, **213**, 65-66.
7. M. Eigen and L. De Maeyer, Untersuchungen über die Kinetik der Neutralisation. I, *Z. Elektrochem., Ber. Bunsen Ges. Phys. Chem.*, 1955, **59**, 986-993.
8. J. Hoigné, H. Bader, W. Haag and J. Staehelin, Rate constants of reactions of ozone with organic and inorganic compounds in water—III. Inorganic compounds and radicals, *Water Res.*, 1985, **19**, 993-1004.
9. R. E. Erickson, L. M. Yates, R. L. Clark and D. McEwen, The reaction of sulfur dioxide with ozone in water and its possible atmospheric significance, *Atmos. Environ.*, 1977, **11**, 813-817.
10. T. Buttersack, I. Gladich, S. Gholami, C. Richter, R. Dupuy, C. Nicolas, F. Trinter, A. Trunschke, D. Delgado, P. Corral Arroyo, E. Parmentier, B. Winter, L. Iezzi, A. Roose, A. Boucly, L. Artiglia, M. Ammann, R. Signorell and H. Bluhm, Direct observation of the complex S (IV) equilibria at the liquid-vapor interface, *Nat. Commun.*, 2024, **15**, 8987.
11. S. Gopalakrishnan, P. Jungwirth, D. J. Tobias and H. C. Allen, Air-liquid interfaces of aqueous solutions containing ammonium and sulfate: Spectroscopic and molecular dynamics studies, *J. Phys. Chem. B*, 2005, **109**, 8861-8872.
12. C. Gottschalk, J. A. Libra and A. Saupe, *Ozonation of water and waste water: A practical guide to understanding ozone and its applications*, John Wiley & Sons, Weinheim, Germany, 2010.
13. W. M. Haynes, ed., *CRC handbook of chemistry and physics*, CRC press, Boca Raton, FL, 2004.
14. J. M. Nielsen, A. W. Adamson and J. W. Cobble, The self-diffusion coefficients of the ions in aqueous sodium chloride and sodium sulfate at 25, *J. Am. Chem. Soc.*, 1952, **74**, 446-451.
15. D. R. Worsnop, M. S. Zahniser, C. E. Kolb, J. A. Gardner, L. R. Watson, J. M. Van Doren, J. T. Jayne and P. Davidovits, The temperature dependence of mass accommodation of sulfur dioxide and hydrogen peroxide on aqueous surfaces, *J. Phys. Chem.*, 1989, **93**, 1159-1172.
16. J. Boniface, Q. Shi, Y. Li, J. Cheung, O. Rattigan, P. Davidovits, D. Worsnop, J. Jayne and C. Kolb, Uptake of gas-phase SO_2 , H_2S , and CO_2 by aqueous solutions, *J. Phys. Chem. A*, 2000, **104**, 7502-7510.
17. D. Donaldson, J. A. Guest and M. C. Goh, Evidence for adsorbed SO_2 at the aqueous-air interface, *J. Phys. Chem.*, 1995, **99**, 9313-9315.

18. W. Li, C. Y. Pak and Y. S. Tse, Free energy study of H₂O, N₂O₅, SO₂, and O₃ gas sorption by water droplets/slabs, *J. Chem. Phys.*, 2018, **148**, 164706.
19. J. Zhong, C. Zhu, L. Li, G. L. Richmond, J. S. Francisco and X. C. Zeng, Interaction of SO₂ with the Surface of a Water Nanodroplet, *J. Am. Chem. Soc.*, 2017, **139**, 17168-17174.
20. M. Baer, C. J. Mundy, T.-M. Chang, F.-M. Tao and L. X. Dang, Interpreting vibrational sum-frequency spectra of sulfur dioxide at the air/water interface: a comprehensive molecular dynamics study, *J. Phys. Chem. B*, 2010, **114**, 7245-7249.
21. M. T. C. Martins-Costa, J. M. Anglada, J. S. Francisco and M. F. Ruiz-Lopez, Photochemistry of SO₂ at the air-water interface: A source of OH and HOSO radicals, *J. Am. Chem. Soc.*, 2018, **140**, 12341-12344.
22. H. Yang, N. J. Wright, A. M. Gagnon, R. B. Gerber and B. J. Finlayson-Pitts, An upper limit to the concentration of an SO₂ complex at the air–water interface at 298 K: infrared experiments and ab initio calculations, *Phys. Chem. Chem. Phys.*, 2002, **4**, 1832-1838.
23. M. D. Willis and K. R. Wilson, Coupled interfacial and bulk kinetics govern the timescales of multiphase ozonolysis reactions, *J. Phys. Chem. A*, 2022, **126**, 4991-5010.
24. R. Dupuy, C. Richter, B. Winter, G. Meijer, R. Schlögl and H. Bluhm, Core level photoelectron spectroscopy of heterogeneous reactions at liquid–vapor interfaces: Current status, challenges, and prospects, *J. Chem. Phys.*, 2021, **154**.
25. F. G. Finger, H. Woolf and C. E. Anderson, A method for objective analysis of stratospheric constant-pressure charts, *Mon. Weather Rev.*, 1965, **93**, 619-638.
26. D. Stemer, T. Buttersack, H. Haak, S. Malerz, H. C. Schewe, F. Trinter, K. Mudryk, M. Pugini, B. Credidio and R. Seidel, Photoelectron spectroscopy from a liquid flatjet, *J. Chem. Phys.*, 2023, **158**.
27. Y.-P. Chang, Z. Yin, T. Balciunas, H. J. Wörner and J.-P. Wolf, Temperature measurements of liquid flat jets in vacuum, *Struct. Dyn.*, 2022, **9**.
28. N. Ottosson, M. Faubel, S. E. Bradforth, P. Jungwirth and B. Winter, Photoelectron spectroscopy of liquid water and aqueous solution: Electron effective attenuation lengths and emission-angle anisotropy, *J. Electron. Specrosc. Relat. Phenom.*, 2010, **177**, 60-70.
29. A. Siebert, K. Goodman and M. Blum, CO₂ absorption process at the liquid–vapor interface of aqueous monoethanol and diethanol amine solutions, *J. Phys. Chem. C*, 2024.
30. M. Wojdyr, Fityk: a general-purpose peak fitting program, *J. Appl. Crystallogr.*, 2010, **43**, 1126-1128.
31. M. O. Krause, Atomic radiative and radiationless yields for K and L shells, *J. Phys. Chem. Ref. Data*, 1979, **8**, 307-327.
32. S. Thürmer, R. Seidel, M. Faubel, W. Eberhardt, J. C. Hemminger, S. E. Bradforth and B. Winter, Photoelectron angular distributions from liquid water: Effects of electron scattering, *Phys. Rev. Lett.*, 2013, **111**, 173005.
33. M. Trzhaskovskaya, V. Nefedov and V. Yarzhemsky, Photoelectron angular distribution parameters for elements Z= 1 to Z= 54 in the photoelectron energy range 100–5000 eV, *At. Data Nucl. Data Tables*, 2001, **77**, 97-159.
34. M. Trzhaskovskaya, V. Nikulin, V. Nefedov and V. Yarzhemsky, Non-dipole second order parameters of the photoelectron angular distribution for elements Z= 1–100 in the photoelectron energy range 1–10 keV, *At. Data Nucl. Data Tables*, 2006, **92**, 245-304.
35. R. Seidel, B. Winter and S. E. Bradforth, Valence electronic structure of aqueous solutions: Insights from photoelectron spectroscopy, *Ann. Rev. Phys. Chem.*, 2016, **67**, 283-305.
36. Z. Tao, J. Goodisman and A.-K. Souid, Oxygen measurement via phosphorescence: reaction of sodium dithionite with dissolved oxygen, *J. Phys. Chem. A*, 2008, **112**, 1511-1518.
37. G. Merényi, J. Lind, S. Naumov and C. von Sonntag, The reaction of ozone with the hydroxide ion: mechanistic considerations based on thermokinetic and quantum chemical

- calculations and the role of HO₄⁻ in superoxide dismutation, *Chem. Eur. J.*, 2010, **16**, 1372-1377.
38. B. Müller and M. R. Heal, The mass accommodation coefficient of ozone on an aqueous surface, *Phys. Chem. Chem. Phys.*, 2002, **4**, 3365-3369.
 39. Z. Wei, Y. Li, R. G. Cooks and X. Yan, Accelerated reaction kinetics in microdroplets: Overview and recent developments, *Ann. Rev. Phys. Chem.*, 2020, **71**, 31-51.
 40. R. M. Onorato, D. E. Otten and R. J. Saykally, Adsorption of thiocyanate ions to the dodecanol/water interface characterized by UV second harmonic generation, *Proc. Natl. Acad. Sci.*, 2009, **106**, 15176-15180.
 41. S.-H. Hsu, F.-Y. Lin, G. G. Huang and Y.-P. Chang, Accelerated sulfur oxidation by ozone on surfaces of single optically trapped aerosol particles, *J. Phys. Chem. C*, 2023, **127**, 6248-6261.
 42. A. M. Prophet, K. Polley, E. K. Brown, D. T. Limmer and K. R. Wilson, Distinguishing surface and bulk reactivity: concentration-dependent kinetics of iodide oxidation by ozone in microdroplets, *J. Phys. Chem. A*, 2024, **128**, 8970-8982.